UNIVERSAL WISER
PUBLISHER

Research Article

Improvement of the Fuzzy Clustering Algorithm for Medical Image Segmentation and Denoising Using Fast Bilateral Filtering

Omid Darvishi[iD]**, Vafa Maihami***[iD]**, Keyhan Khamforoosh**[iD]

Department of Computer Engineering, Sa.C., Islamic Azad University, Sanandaj, Iran
E-mail: Maihami@iau.ac.ir

Abstract: Medical image analysis often faces challenges due to noise, which can obscure crucial diagnostic information and hinder precise segmentation. Traditional denoising methods often fail to effectively suppress noise while preserving image details, resulting in blurred or overly smoothed outputs. To address this, we propose an improved fuzzy clustering algorithm that introduces an innovative integration of fast bilateral filtering and adaptive parameter tuning, offering superior noise reduction and enhanced medical image segmentation accuracy. Our method introduces a novel combination of fast bilateral filtering and an enhanced fuzzy C-means (FCM) algorithm, which effectively balances noise suppression and detail preservation, outperforming existing methods in both accuracy and efficiency. The fast bilateral filter efficiently preserves edge details while reducing spatial and local intensity variations, serving as a robust preprocessing step that mitigates noise-induced clustering errors. Additionally, we introduce an innovative strategy that calculates the absolute difference between the original and filtered images to enhance clustering accuracy in noisy environments. To improve convergence speed and computational efficiency, we refine the FCM objective function by incorporating a logarithmic summation of membership degrees from previous iterations, reducing iteration counts and accelerating convergence. Finally, we apply sharpening and median filtering techniques to refine segmentation outputs and enhance detail clarity. Experimental results on benchmark medical images demonstrate that our proposed method achieves superior noise suppression, improved segmentation accuracy, and faster convergence compared to conventional FCM and recent denoising techniques.

Keywords: fast bilateral filtering, fuzzy clustering, medical image segmentation, noise reduction in medical images, edge preservation, image preprocessing

MSC: 65L05, 34K06, 34K28

Abbreviation

CNN	Convolutional Neural Network
CT	Computed Tomography
FCM	Fuzzy C-Means
IFCM-dmf	Improvement of the Fuzzy Clustering Algorithm for Medical Image Segmentation and Denoising Using Fast Bilateral Filtering

MI	Mean Intersection
MRI	Magnetic Resonance Imaging
PSNR	Peak Signal-to-Noise Ratio
SA	Segmentation Accuracy
SSIM	Structural Similarity Index Measure

1. Introduction

Image processing plays a crucial role in enhancing the quality of visual data for a wide range of applications, including medical diagnostics, satellite imaging, and environmental monitoring. However, one of the major challenges in image processing is the presence of noise, which can be introduced during image acquisition, storage, transmission, or compression [1–4]. Noise not only diminishes the visual quality of an image but also impacts key image processing tasks such as segmentation, content recognition, and interpretation. This is particularly critical in medical imaging, where image clarity directly affects the accuracy of disease diagnoses and clinical decision-making. Therefore, effective denoising techniques that preserve important image features such as edges and textures while removing noise are essential for successful image processing applications.

A digital image is typically a two-dimensional numerical representation of data, and high-resolution inputs are required for precise analysis in fields such as medicine and satellite imaging [4, 5]. To address the issue of degraded image quality due to noise, two main approaches are commonly used: hardware-based methods, which modify camera sensor structures, and software-based methods, which employ advanced algorithms and filters. Hardware-based methods are often impractical due to high implementation costs and technological limitations [6]. In contrast, software-based methods, which are more feasible, aim to eliminate noise while preserving critical image features such as edges and textures [7, 8].

In medical imaging, noise presents a particularly significant challenge. Medical images are inherently complex and often contaminated with unpredictable noise, which can obscure vital details and potentially lead to misdiagnoses [7, 9–15]. Over the past two decades, automatic noise reduction has become a key component in medical image processing, significantly supporting accurate disease diagnosis [10, 16, 17]. However, designing denoising methods that are both fast and precise remains a major challenge due to the diverse and unpredictable nature of noise in medical images [14].

Given the limitations of traditional denoising techniques, such as the sensitivity of fuzzy C-means (FCM) to noise and its inability to account for local pixel relationships [18, 19], and the challenges faced by convolutional neural networks (CNNs), such as overfitting and limited generalizability to new noise types [20], a more effective solution is needed. This paper introduces a novel method that combines the strengths of optimized fast bilateral filtering and fuzzy clustering to overcome these challenges, ensuring both high-quality denoising and reduced processing time.

The proposed method consists of four key steps:

1. **Optimized fast bilateral filter with automatic parameter selection:** This filter preserves image edges while extracting local information and spatial intensity, with automatic parameter adjustment to reduce processing time and enhance noise reduction accuracy.

2. **Image difference calculation:** The image is refined by calculating the absolute difference between the original and the bilaterally filtered images, which constrains the traditional FCM algorithm.

3. **Incorporation of composite noise:** This step improves noise separation and segmentation quality compared to existing methods.

4. **Final enhancement:** A sharpening and median filter is applied to further refine the output image.

The reason for using this method lies in its ability to combine the efficiency of the fast bilateral filter with the robust noise-handling capabilities of fuzzy clustering. By incorporating automatic parameter selection, the method adapts to different types of noise, significantly reducing processing time and improving overall denoising performance. This makes the approach highly suitable for real-time applications in medical diagnostics, where quick and accurate results are essential.

The contributions of this research are threefold:

• **Enhanced denoising efficiency:** The optimized fast bilateral filter significantly improves the precision of noise reduction while reducing processing time, making it ideal for real-time medical applications.

• **Novel fuzzy clustering approach:** The modified fuzzy clustering technique introduces new methods for handling noisy images, resulting in more accurate and faster segmentation.

• **Impact on medical imaging:** Experimental results demonstrate substantial improvements in medical image quality, reducing noise and enhancing segmentation, with direct implications for improving disease diagnosis and clinical decision-making.

Real-world applications: The findings of this research have practical applications in enhancing the accuracy of medical diagnostics in imaging modalities such as MRI and CT scans, reducing noise in satellite imagery, and even improving image quality in industrial and commercial surveillance systems. These techniques are particularly relevant for real-time applications where fast and accurate image processing is crucial, such as in hospitals, space industries, and surveillance environments.

This paper is organized as follows: Section 1 provides the introduction; Section 2 presents background information on FCM and related works; Section 3 explains the proposed image denoising method; Section 4 presents experimental results and sensitivity analysis; and Section 5 concludes the paper.

2. Related works and background

This section reviews the fuzzy c-means (FCM) algorithm and related works.

2.1 *Background*

The computational complexity of the standard bilateral filtering method is high. To address this issue, a fast approximation method utilizing signal processing techniques is employed, which reduces the complexity to an acceptable level [21]. This can be represented by the following equation.

$$\begin{pmatrix} w_p^{bf} i_p^{bf} \\ w_p^{bf} \end{pmatrix} = \sum_{q \in S} \sum_{\zeta \in R} G_{\sigma_s}(\| p - q \|) G_{\sigma_r}(|i_p - \zeta|) \delta(\zeta - i_q) \begin{pmatrix} w_q i_q \\ w_q \end{pmatrix} \tag{1}$$

$$I_p^{bf} = \frac{w_p^{bf} i_p^{bf}}{w_p^{bf}} \tag{2}$$

• w_p^{bf} and w_p^{bf}: These symbols represent the weights corresponding to pixels p and q after applying the bilateral filter. These weights are computed based on the spatial distance and intensity difference between different pixels. Specifically, the bilateral filter applies weighting based on spatial and color similarity between the target pixel and neighboring pixels.

• i_p^{bf} and i_q: These represent the intensity (or color) values of pixels p and q in the image. i_p^{bf} is the intensity of pixel p after applying the bilateral filter, and i_q is the intensity of pixel q in the original image.

• $G_{\sigma_r}(|i_p - \zeta|)$: This is the spatial kernel of the bilateral filter, directly related to the spatial distance between pixels p and q. The parameter σ_s controls the strength of the spatial distance effect, meaning that the greater the distance between pixels, the less weight is applied to that pixel.

• $G_{\sigma_r}(|i_p - \zeta|)$: This is the range kernel of the bilateral filter, depending on the intensity difference between pixels. $i_p - \zeta$ represents the intensity difference between pixel p and the intensity ζ which could be the intensity of a neighboring pixel or a reference pixel. The parameter σ_r controls the strength of this intensity difference effect. The greater the intensity difference, the less impact it has on the weight.

• $\zeta - i_q$: This is a Kronecker delta function that compares ζ and the intensity i_q of pixel q. This function returns 1 if ζ is equal to the intensity of pixel q, and 0 otherwise.

- $w_q i_q$ and w_q: These represent the weights and intensity of pixel q in the final filtering result. These values are generally computed using the sum of weights and intensities.

The main objective of Equation (1) is to combine spatial and intensity information for filtering the image, reducing noise while preserving details, especially removing noise caused by intensity and spatial distance differences.

The parameters of the fast bilateral filter are shown in Table 1. Also, different parts of the fast bilateral filter are shown in Figure 1. The longitudinal axis involves the pixel position (p) and space (s_s), and the latitudinal axis involves image intensity (I_p) and range (s_r). q is a pixel in the proximity of p, and I_q represents the brightness of pixel q. G_{σ_s} ($\| p - q \|$) concerns the space section, and $G_{\sigma_r} (|i_p - \zeta|) \delta (\zeta - i_q)$ pertains to the range section. The product $G_{\sigma_s} (\|p - q\|) G_{\sigma_r} (|i_p - \zeta|) \delta (\zeta - i_q)$ indicates the distance from p to q.
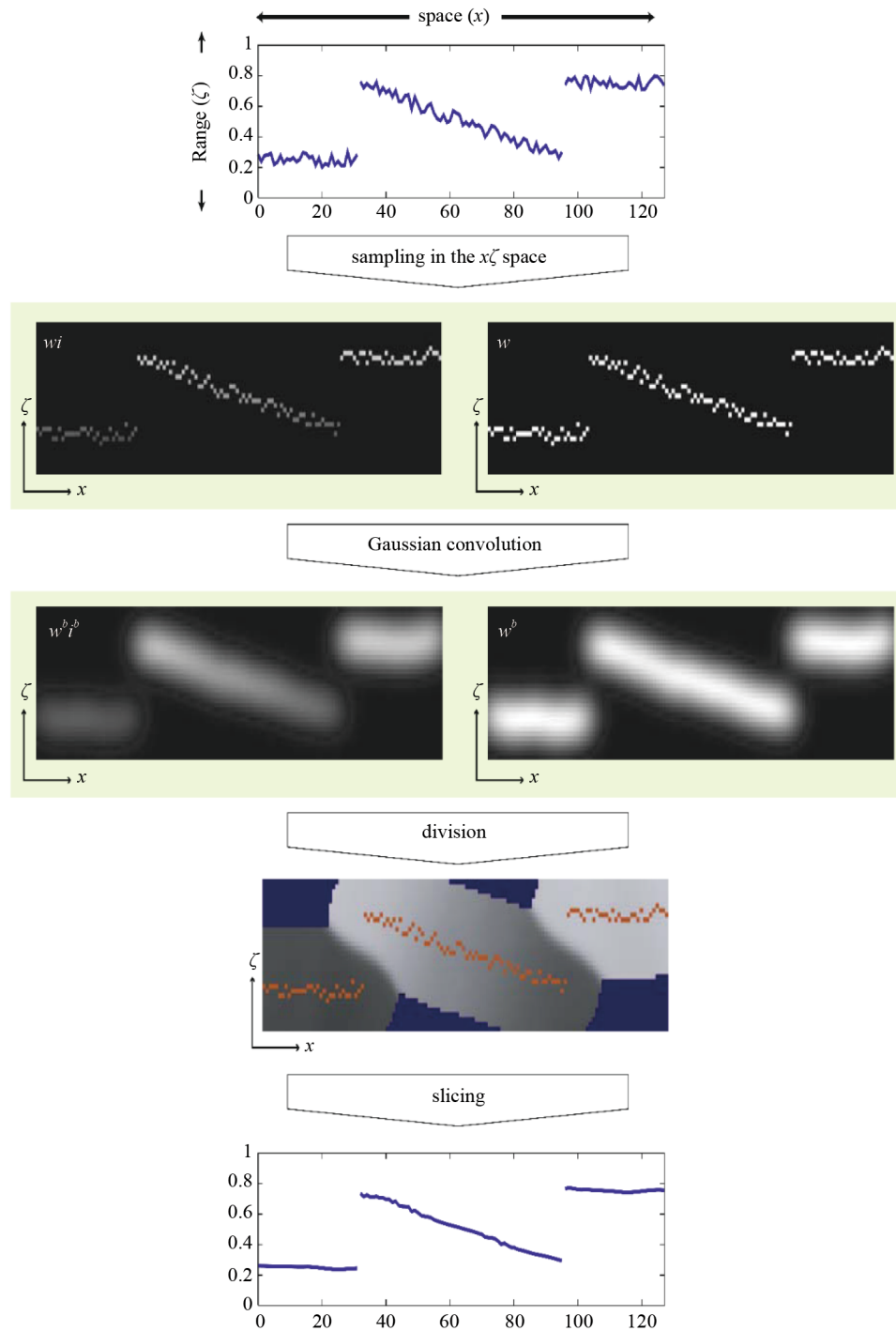
Table 1. Parameters of the fast bilateral filter

Parameters	Index
$\mathscr{S}$	Spatial domain
I, W	2D functions defined on $\mathscr{S}$
$\mathbf{p}, \mathbf{C}$	Vectors
$\| \mathbf{x} \|$	$\mathbf{L_2}$ norm of vector $\mathbf{x}$
$\otimes$	Convolution operator
G_σ	1D Gaussian: $\mathbf{x} \mapsto \exp\left(-\dfrac{\mathbf{x}^2}{2\sigma^2}\right)$
s_s, s_r	Sampling rates (space and range)
I^b	Result of the bilateral filter
$\mathscr{R}$	Range domain
i, w	3D functions defined on $\mathscr{S} \times \mathscr{R}$
$\mathbf{p} \in \mathscr{S}$	Pixel position (2D vector)
$I_\mathbf{p} \in \mathscr{R}$	Image intensity at $\mathbf{p}$
$\delta(x)$	Kronecker symbol ($\mathbf{1}$ if $\mathbf{x} = \mathbf{0}$, $\mathbf{0}$ otherwise)
g_{σ_s, σ_r}	3D Gaussian: $(\mathbf{x}, \zeta) \in \mathscr{S} \times \mathscr{R} \mapsto \exp\left(-\dfrac{\mathbf{x} \cdot \mathbf{x}}{2\sigma_\mathbf{s}^2} - \dfrac{\zeta^2}{2\sigma_\mathbf{r}^2}\right)$
σ_s, σ_r	Gaussian parameters (space and range)
W^b	Normalization factor
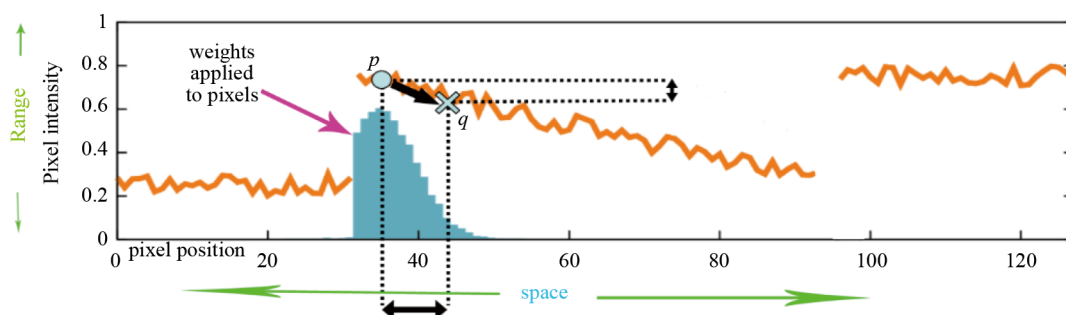
Figure 1. Different parts of the fast bilateral filter

The result of the application of the fast bilateral filter is shown in Figure 2.

Figure 2. Block diagram of the fast bilateral filter

The algorithm of fast bilateral filter method proposed in [21] is shown in Algorithm 1.

Algorithm 1 The fast bilateral filter method proposed in [21]

Input: Image **I**

Gaussian parameters σ_s, σ_r

Sampling rates s_s, s_r

Output: Filtered image $\mathbf{I}^b$

Initialization:

    Set all $\mathbf{w}_\downarrow \mathbf{i}_\downarrow$ and $\mathbf{w}_\downarrow$ values to 0

Compute minimum intensity value:

$$I_{\min} \leftarrow \min_{(X,Y) \in \mathscr{S}} I(X, Y)$$

for *each pixel* $(X, Y) \in \mathscr{S}$ *with intensity* $I(X, Y) \in \mathscr{R}$ **do**

    (a) Compute homogeneous vector:

$$(wi, w) \leftarrow (I(X, Y), 1)$$

    (b) Compute downsampled coordinates:

$$(x, y, \zeta) \leftarrow \left(\left\lfloor \frac{X}{s_s} \right\rfloor, \left\lfloor \frac{Y}{s_s} \right\rfloor, \left\lfloor \frac{I(X, Y) - I_{\min}}{s_r} \right\rfloor \right)$$

    (c) Update downsampled $\mathscr{S} \times \mathscr{R}$ space:

$$\begin{pmatrix} \mathbf{w}_\downarrow \mathbf{i}_\downarrow(x, y, \zeta) \\ \mathbf{w}_\downarrow(x, y, \zeta) \end{pmatrix} \leftarrow \begin{pmatrix} \mathbf{w}_\downarrow \mathbf{i}_\downarrow(x, y, \zeta) \\ \mathbf{w}_\downarrow(x, y, \zeta) \end{pmatrix} + \begin{pmatrix} wi \\ w \end{pmatrix}$$

end

for *each pixel* $(X, Y) \in \mathscr{S}$ *with intensity* $I(X, Y) \in \mathscr{R}$ **do**

    (a) Tri-linear interpolation:

$$W^b I^b(X, Y) \leftarrow \text{interpolate} \left(\mathbf{w}_\downarrow^b \mathbf{i}_\downarrow^b, \frac{X}{s_s}, \frac{Y}{s_s}, \frac{I(X, Y)}{s_r} \right)$$

$$W^b(X, Y) \leftarrow \text{interpolate} \left(\mathbf{w}_\downarrow^b, \frac{X}{s_s}, \frac{Y}{s_s}, \frac{I(X, Y)}{s_r} \right)$$

    (b) Normalization:

$$I^b(X, Y) \leftarrow \frac{W^b I^b(X, Y)}{W^b(X, Y)}$$

end

2.1.1 *FCM algorithm*

The FCM algorithm was initially proposed by Dunn [22] and then improved by Bezdek [23]. This method presents a new perspective in clustering based on fuzzy logic [24]. In this novel perspective, the data are members of all the clusters with membership factors ranging between zero and one rather than members of single clusters, and we seek these factors in this type of clustering. In conventional methods, the final result is a $1 \times N$ matrix, where N represents the number of data, and each cell contains the corresponding data cluster label. In this method, however, the final result is a $k \times N$ matrix, where k represents the number of clusters, and each row contains the membership factors of the data corresponding to the cluster. Clearly, the horizontal sum of the values on each row (membership factors of specific data) is one. A common method for achievement of non-fuzzy solutions based on the final results of the fuzzy algorithm is to label the data based on the factor with the maximum value in the data. Equation (3) is the basic equation in the fuzzy method [22]:

$$O_{\text{FCM}}^{(z)} = \sum_{i=1}^{K} \sum_{j=1}^{N} \left(u_{ij}^{(z)} \right)^m \| x_j - c_i^{(z)} \|^2, \quad \sum_{i=1}^{K} u_{ij}^{(z)} = 1 \tag{3}$$

where m is a real number greater than one, and u_{ij} is the membership degree of x_j in the ith cluster. x_j is, in turn, the jth d-dimensional data under investigation, and c_i is the d-dimensional center of the ith cluster. $\| * \|$ represents any common method of measuring the similarity between x_j and c_i. In the fuzzy clustering method, the cluster centers (c_i) and membership degrees (u_{ij}) are iteratively updated based on Equations (4) and (5), respectively, until the stopping condition is met. In this condition, ε has an agreed-on value far smaller than one, which can be replaced according to the data type and clustering accuracy. Clearly, the degree of membership will become more accurate, and runtime will become longer as the above value tends to zero [22].

$$u_{ij}^{(z)} = \frac{1}{\sum_{r=1}^{K} \left(\frac{\| x_j - c_i^{(z)} \|}{\| x_j - c_r^{(z)} \|} \right)^{\frac{2}{m-1}}} \tag{4}$$

$$c_i^{(z)} = \frac{\sum_{j=1}^{N} \left(u_{ij}^{(z)} \right)^m}{\sum_{j=1}^{N} \left(u_{ij}^{(z)} \right)^m} \tag{5}$$

The FCM algorithm is shown in Algorithm 2.
Algorithm 2 FCM algorithm
Input: Number of clusters **k**
Weighting exponent **m**
Minimum error ε
Initialize:
   1. Set all center vectors $\mathbf{c}_i^{(0)} \leftarrow \mathbf{0}$
   2. Randomize membership degrees $\mathbf{u}_{ij}^{(0)}$
   3. Set loop counter $z \leftarrow 1$

repeat

  Iteration z:

   a. Update centers: $\mathbf{c}_i^{(z)} \leftarrow \dfrac{\sum_{j=1}^{n}(\mathbf{u}_{ij}^{(z-1)})^m \mathbf{x}_j}{\sum_{j=1}^{n}(\mathbf{u}_{ij}^{(z-1)})^m}$ (Equation (5))

   b. Update memberships: $\mathbf{u}_{ij}^{(z)} \leftarrow \left[\sum_{l=1}^{k}\left(\dfrac{\|\mathbf{x}_j - \mathbf{c}_i^{(z)}\|}{\|\mathbf{x}_j - \mathbf{c}_l^{(z)}\|}\right)^{2/(m-1)}\right]^{-1}$ (Equation (4))

   c. Update objective: $\mathbf{O}_{FCM}^{(z)} \leftarrow \sum_{i=1}^{k}\sum_{j=1}^{n}(\mathbf{u}_{ij}^{(z)})^m \|\mathbf{x}_j - \mathbf{c}_i^{(z)}\|^2$ (Equation (3))

   d. Increment counter: $z \leftarrow z + 1$

until $\left\|\mathbf{O}_{FCM}^{(z)} - \mathbf{O}_{FCM}^{(z-1)}\right\| < \varepsilon$ **and** $z > 1$;

Output: Final membership degrees $\mathbf{u}_{ij}^{(z)}$.

2.2 Related works

Researchers use various methods to mitigate the impact of noise in clustering, which are categorized into five classes based on different techniques: 1-histogram clustering, 2-clustering using prior probability functions, 3-kernel-based clustering, 4-clustering based on local intensity information, and 5-intuitionist fuzzy clustering.

In the adaptive possibilistic fuzzy FCM-segmentation (APFFCM-S) model [25], propose a new fuzzy clustering to improve resistance and resolve the parameter selection problem. First, a new regulating method is presented that can resolve the problem of time in fuzzy clustering. The next step involves a modification of the objective function by combining local weight information given the interaction between current and neighboring pixels and including the constraint on maximum weight for resolving the above problem. In the last step, the adjacent image is constructed through constraints on the current pixel and fuzzy local spatial information thereon, and the clustering center is modified through modification of the current image pixels. In this method, spatial and local intensity information is used, and the major drawbacks include huge time consumption and low speed.

In the bias correction embedded fuzzy c-means with spatial constraints (BCEFCM-S) model [26], propose method based on fuzzy c-means to segment images, including both bias correction and denoising. Bilateral filters are used there to correct the bias value and spatial constraints are used in the memberships to remove noise, hence the title bias correction embedded fuzzy c-means with spatial constraints (BCEFCM-S). The major drawback of the method is that it disregards spatial information.

The rough fuzzy C-means with spatial constraints (RFCMSC) model [27] introduces a fuzzy c-means algorithm enhanced with spatial constraints for brain MRI segmentation. By integrating fuzzy set and rough set theories, the model effectively addresses uncertainty, overlap, and missing details in MRI data. Although spatial constraints improve noise management by considering neighboring pixels during labeling, the method's primary limitations are its high computational cost and slow processing speed.

In the super-pixel based fast fuzzy C-means (SFFCM) model [28], propose a method of fast FCM clustering based on super pixels, which is significantly faster and more powerful than state-of-the-art clustering algorithms for segmentation of color images. To obtain better local spatial neighborhoods, a multi-scale morphological gradient reconstruction operation is first defined to provide a super pixel image with accurate counters. Moreover, the original color image is effectively simplified based on the obtained super pixel image, and the histogram is easily calculated through enumeration of pixels in each region of the super pixel image. Finally, FCM is implemented on the super pixel image using the histogram parameter

to obtain the ultimate segmentation results. The major drawback of the method is that there is no spatial information in the process of histogram clustering.

The fuzzy local dual neighborhood information C-means (FLDNICM) model [29] introduces a c-means clustering method that leverages local information from two fuzzy neighborhoods for remote-sensing image classification. It employs a weighted fuzzy factor, derived from a spatial gravity model, to estimate spatial constraints accurately. Additionally, a fuzzy prior probability function enhances noise resistance by combining pixel and neighborhood data. Both components are parameter-free and adapt to image content. Despite improving edge clarity, the method relies on assumptions and faces challenges with uncertainty.

In the robust fuzzy C-means with local grey information (RFCMLGI) model [30], the fuzzy c-means algorithm is modified in different ways to resolve the problem of image segmentation. However, virtually all extensions need to set a minimum of one parameter, causing a problem depending on the type of image. To resolve the issue, a powerful algorithm of fuzzy clustering totally independent of the type of noise and free of experimental parameters is proposed in this method that involves local spatial and grey area information. The presented approach is not restricted to the original FCM method and is not considered for the number of iteration steps, which makes up its main weakness.

The adaptive robust kernel-based fuzzy C-means (ARKFCM) model [31] introduces a regular kernel-based clustering method for brain image segmentation, utilizing three approaches based on local average, median filter, and weighted grey scales. These methods extract local contextual information by analyzing neighboring grey scales. Key advantages include adaptability to local settings, improved detail preservation, independent clustering parameters, and reduced computational costs. However, its effectiveness in noisy image segmentation remains limited.

In the paper [12], a method for removing Poisson noise from X-ray medical images is employed using the finite impulse response (FIR) filter embedded in the Wiener algorithm, which is designed by the adaptive search optimization (ASO) optimization algorithm. X-ray imaging often introduces various types of noise, such as Poisson noise, which can lead to image distortion. By calculating the local optimal average and local optimal variance values using the optimization matrix of FIR filter coefficients as input parameters, these values are then transferred to the standard Wiener filter layer, resulting in a significant reduction of Poisson noise. However, a major drawback of this method is the occurrence of blurring and residual image noise.

In [7], the estimation of multi-filters combining large datasets is examined. Edge loss is a crucial factor affecting both images and signals, as it is widely recognized that limited information leads to edge blurring. In this method, the objective function incorporates spatial information from the surrounding area of noisy data by utilizing multiple filters and combining their outputs. The objective function is then optimized using the flower pollination algorithm (FPA) for different sizes of filter windows. However, a major issue with this method is that it tends to cause blurring, resulting in the removal of image details while leaving a certain level of noise.

The method proposed by Shi et al. [32] introduces a geometry-consistent fuzzy clustering model that employs a gradient-preserving weight in membership reconstruction to maintain alignment with the original data. While this approach enhances clustering performance, its reliance on combining membership results from multiple algorithms may lead to loss of image details and reduced edge detection accuracy. Moreover, the method's limited focus on geometric consistency with the original image can further affect segmentation precision.

Cui et al. present an innovative framework called fast fuzzy c-means-Markov random field (FFCM-MRF) for precise segmentation of cerebral vasculature in time-of-flight-magnetic resonance angiography (TOF-MRA) images [33]. By combining fast fuzzy c-means clustering with MRF optimization, they effectively reduce segmentation noise and enhance vessel continuity. The main issue with this method lies in its reliance on combining fuzzy clustering for precise segmentation of cerebral vascular environments in TOF-MRA images. This approach leads to loss of details from the original image and inaccurate detection of edges. Additionally, the geometric inconsistency between membership vectors and the original image results in segmentation outputs that do not accurately reflect the underlying spatial structures of the data.

In this article proposed by Wei et al. [34], a new method for image segmentation, termed FSC_LNML, is introduced. This approach combines local and non-local spatial information with the mean membership relationship in the fuzzy C-means (FCM) algorithm to enhance segmentation quality. By employing a customized algorithm for each image

dimension, it effectively suppresses noise and enhances segmentation accuracy, especially for color images. One of the main issues of this method is its potential high computational complexity, especially when dealing with large images. Additionally, sensitivity to algorithm parameter tuning and dependence on the quality and type of the image are other concerns.

Song et al. present a novel algorithm, adaptive-FCM (AFCM), for image segmentation, surpassing limitations of prior methods like FCM [35]. AFCM integrates a superpixel representation to mitigate computational complexities and introduces a novel distance metric alongside fuzzy weight management, thereby significantly enhancing the precision and efficiency of feature clustering in image segmentation. The primary issues with the AFCM algorithm include sensitivity to initial parameters, increased computational complexity, the potential loss of accurate image information due to the use of superpixel representation, the need for precise adjustment of fuzzy weights, and the possibility of not achieving improvements in final accuracy and efficiency.

The emphasis in this article, prepared by Bose et al. [36], lies in the critical role of image processing techniques in medical research, particularly in the precise segmentation of brain MRI images. The challenges associated with manual segmentation and the effects of noise and field deviations in MRI images are highlighted. Advanced methods such as the entropy-based fuzzy membership function (EMT2FCM) are introduced to address these challenges. Incorporating entropy into the Gaussian membership function significantly enhances segmentation accuracy. Overall, the article underscores the importance of employing advanced techniques in medical image segmentation. The main issue with this method is the requirement for precise determination of parameters such as thresholds for segmentation and selection of appropriate features for classification. Additionally, computational complexity and sensitivity to image quality and artifacts are other issues associated with it.

Aetesam and Maji propose a variational approach for denoising magnetic resonance images (MRIs) that are influenced by Rician noise dependent on the signal [37]. This model utilizes approximate posterior variances and a hyper-Laplacian distribution, demonstrating high efficiency in noise reduction while preserving image details. However, the complexity of parameter tuning and the need for sufficient training data may limit its effectiveness in certain conditions.

Xu et al. introduce a convolutional neural network (CNN) inspired by wavelet analysis for image denoising [38]. By employing wavelet decomposition, this model effectively enhances image quality and significantly reduces noise. A primary challenge of this approach is the potential increase in computational complexity, which may affect the model's overall performance, particularly when handling large images.

Zhang et al. present the denoising swin transformer (DnST) model for denoising low-dose computed tomography (CT) images [39]. This model integrates a perceptual loss function and modifies the network structure to effectively reduce noise while protecting structural integrity and crucial image information. A notable challenge of this method lies in the requirement for precise parameter tuning to achieve optimal results.

Torun et al. introduce a self-modulating convolutional neural network (SM-CNN) for hyperspectral image denoising [40]. This model features a novel block, termed the spectral self-modulating residual block (SSMRB), which adaptively transforms features based on adjacent spectral data, enhancing the network's ability to manage complex noise. However, it may require diverse and ample training data to demonstrate optimal performance.

Zhang et al. propose SGDFormer, a transformer-based architecture for cross-spectral stereo image guided denoising [41]. This model integrates correspondence modeling and feature fusion within a unified network framework. The main challenge of this approach is the need for high-quality stereo data for effective training and evaluation.

Feruglio et al. present a block matching 3D (BM3D) random noise filtering technique to enhance image quality in absorption optical projection tomography (OPT) [42]. By applying the BM3D filter to each projection prior to three-dimensional reconstruction, this method significantly improves the signal-to-noise ratio, especially in cases affected by substantial noise. However, while the approach effectively reveals image details hidden by noise, a key challenge is the increased computational complexity, which may impact performance, particularly when dealing with large datasets.

Zhao et al. introduced a modified DnCNN model for denoising ultra-low-dose CT scans [43]. By simulating paired ultra-low-dose and high-quality reference images, this model significantly improves image quality, increasing the peak signal-to-noise ratio by up to 8 dB and reducing the underestimation of emphysema. However, while outperforming

previous models, the method still faces challenges such as over-smoothing, which may obscure finer details in some cases. Nevertheless, this issue did not negatively impact the clinical conclusions.

Chen et al. introduce a residual encoder-decoder convolutional neural network (RED-CNN) for low-dose CT imaging, highlighting the potential risks associated with X-ray radiation [44]. Current low-dose CT methods often rely on raw data that are not readily accessible and face challenges in effectively removing noise while preserving structural details. The proposed RED-CNN integrates autoencoders, deconvolutional networks, and shortcut connections. Following patch-based training, this method demonstrates competitive performance against state-of-the-art techniques, particularly excelling in noise suppression, structural preservation, and lesion detection.

In the DNetUnet model [45], a new convolutional neural network architecture is proposed that integrates U-Nets with multiple down-sampling levels and a novel dense block for improved feature extraction. This architecture is designed for semi-supervised learning, enabling the model to harness knowledge from labeled datasets while simultaneously enhancing its generalization capabilities using unlabeled data. Moreover, DNetUnet incorporates a distillation technique aimed at improving performance on mobile platforms. The model is particularly effective for processing large medical images and is best utilized on supercomputing AI training servers. Despite its advanced performance, the method demands considerable computational resources and may face challenges in real-time applications due to its processing requirements.

In the adaptive fully-dual (AFD) neural network model [46], an adaptive fully dense architecture is proposed specifically for CT image segmentation. This model enhances the traditional UNet structure by introducing horizontal connections that allow for adaptive extraction of various features across all layers. To further improve performance, ensemble training is employed, which focuses on extracting edge information through multiple rounds of training. The method has been validated on two datasets: a natural scene image dataset and a liver cancer CT image dataset. Experimental results indicate that this model outperforms state-of-the-art segmentation techniques, demonstrating its efficacy in handling complex boundaries in CT images.

Younas et al. proposed a content-based image retrieval (CBIR) framework that leverages user feedback to enhance retrieval accuracy and provide query suggestions for improved search results. This method effectively captures user intent, improving performance in large and diverse image datasets. The framework demonstrates strong scalability and efficient handling of vast image repositories. However, the reliance on relevance feedback may require additional user interaction, which could limit automation in fully autonomous systems [47].

Ravichandran introduced an automatic license plate recognition (ALPR) method leveraging deep learning and computer vision techniques, specifically designed to handle noisy images in real-world scenarios. The proposed approach incorporates various preprocessing techniques, such as noise removal algorithms and extended hair-removal algorithms, before applying deep learning models, including the latest version of YOLO v8. The results demonstrate that the proposed model outperforms existing state-of-the-art methods. However, its performance may require further enhancement when dealing with highly complex environments featuring challenging lighting conditions and unfavorable viewing angles [48].

Citroni et al. provides a comprehensive review on optimizing energy consumption in wireless sensor systems. It emphasizes the importance of utilizing ultra-low-power design techniques (ULPDT) and energy management to extend the lifespan of wireless devices. This topic is particularly relevant in medical applications, as many imaging devices and medical sensors are used in remote environments or conditions with limited energy resources. In such settings, in addition to effectively removing noise and enhancing image quality, noise reduction methods must be designed to consume minimal energy while ensuring high performance, ensuring the reliable and continuous operation of these devices [49].

Table 2 shows the advantages and drawbacks of each of the examined methods.

Table 2. Comparison of the examined previous works

Model	Year	Advantages and drawbacks	Researchers
APFFCM-S [25]	2020	Advantages: Use of spatial and local intensity information. Drawbacks: Huge time consumption and low speed.	Wu C, Chen Y
BCEFCM-S [26]	2020	Advantages: Use of local intensity information. Drawbacks: Disregarded spatial information.	Feng C, Li W, Hu J, Yu K, Zhao D
RFCMSC [27]	2019	Advantage: Use of spatial and local intensity information. Drawbacks: Huge time consumption and low speed.	Halder AAN
SFFCM [28]	2019	Advantage: Consideration of local information prior to clustering and very high speed. Drawbacks: Absence of all spatial information.	Lei T, Jia X, Zhang LY, He H, Meng H, Nandi AK
FLDNICM [29]	2018	Advantages: Use of prior probability functions such as the random hidden Markov chain as proper means of removing uncertainty. Drawbacks: Assumptions made as basis.	Zhang H, Bruzzone L, Shi W, Hao M, Wang Y
RFCMLGI [30]	2016	Advantages: Use of spatial and local intensity information in optical and noisy image segmentation. Drawbacks: Unlimited use of original FCM, disregarded for the number of iteration steps.	Barrah H, Cherkaoui A, Sarsri D
ARKFCM [31]	2015	Advantages: Designed to confront problems of nonlinear classification. Drawbacks: Little progress made in noisy image segmentation.	Elazab A, Wang C, Jia F, Wu J, Li G, Hu Q
Medical X-ray [12]	2023	Advantages: removing Poisson noise in X-ray images. Drawbacks: Blurring and residual image noise.	Göreke V
FPAENH [7]	2023	Advantages: using spatial information and combining different filters to remove noise from Alzheimer's images. Drawbacks: blurring and removing image details and leaving a percentage of noise.	Srivastava V
$GCFE_s$ [32]	2023	Advantages: A geometrically consistent fuzzy clustering model with gradient-preserving weight for image segmentation. Drawbacks: Reliance on fuzzy clustering ensemble and loss of image details.	Shi P, Guo L, Cui H, Chen L
AFD neural network [45]	2020	Advantages: Adaptive feature extraction, effective for complex CT images, superior performance compared to state-of-the-art methods. Drawbacks: Requires extensive training data and computational resources.	Wang EK, Chen CM, Hassan MM, Almogren A
DnetUnet [46]	2021	Advantages: Combines U-Nets at various down-sampling levels, employs semi-supervised learning for enhanced generalization, integrates distillation for mobile platform performance. Drawbacks: Requires significant computational resources, best applied using a supercomputing AI training server.	Tseng KK, Zhang R, Chen CM, Hassan MM
Deep variational MRI denoising [37]	2024	Advantages: Effective at reducing Rician noise and preserving details. Drawbacks: Complex parameter tuning, requires large datasets.	Aetesam H, Maji SK
Wavelet analysis model inspired CNN [38]	2024	Advantages: Enhances image quality through waveletdecomposition. Drawbacks: Computational complexity, challenging for large images.	Xu et al.
Denoising swin transformer (DnST) [39]	2024	Advantages: Reduces noise while protecting structure and critical information. Drawbacks: Sensitive to parameter tuning.	Zhang et al.
Hyperspectral image denoising via SM-CNN [40]	2024	Advantages: Adapts to complex noise using spectral data. Drawbacks: Requires diverse training data for optimal results.	Torun et al.
SGDFormer: Transformer-based architecture [41]	2025	Advantages: Integrates correspondence modeling and feature fusion for artifact-free denoising. Drawbacks: Requires high-quality stereo data.	Zhang et al.

3. Proposed method

3.1 *Methodology*

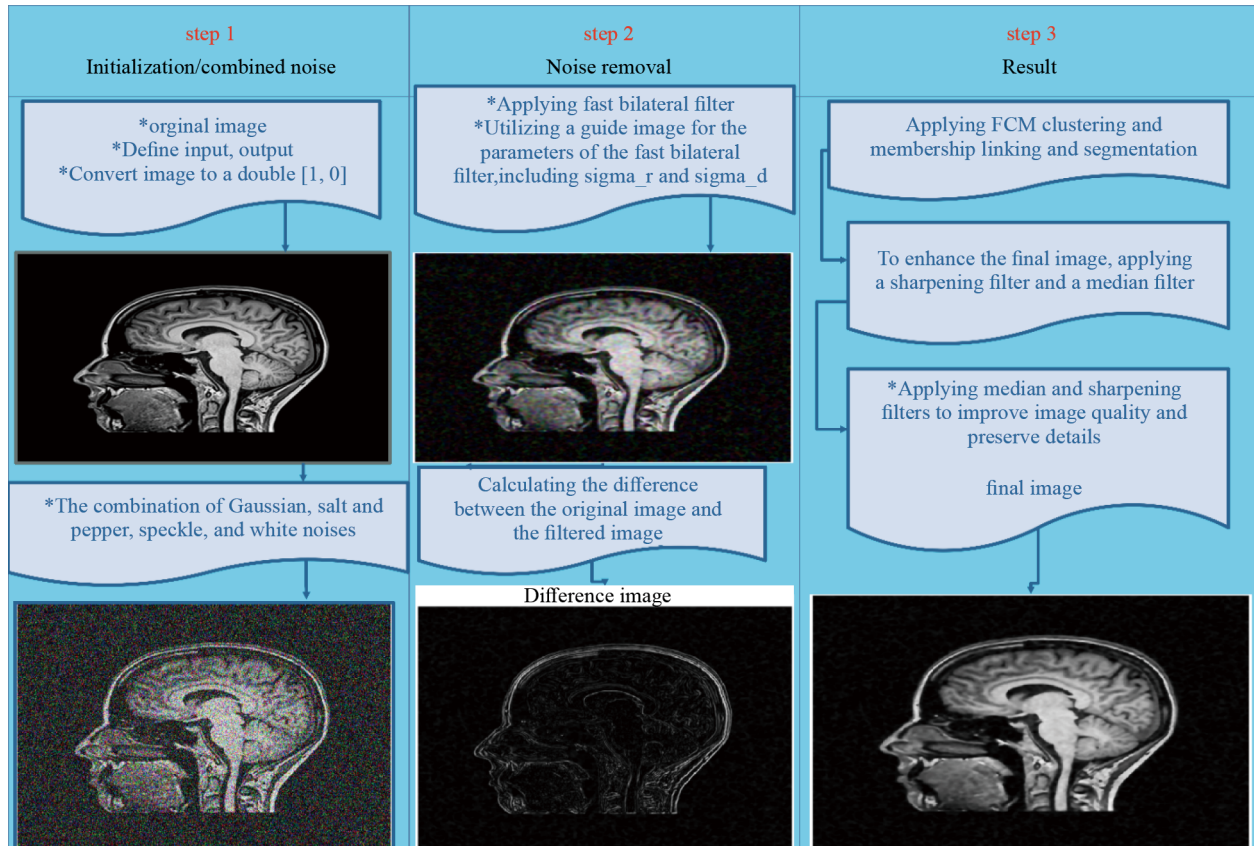The general steps of the proposed method are shown in Figure 3.

Figure 3. The structure of proposed method

According to the diagram, the process begins with reading the input image and converting it to a double format. Next, four types of noise are introduced to the original image, followed by fast bilateral filtering to maintain edge details. The difference between the original and filtered images is then computed, and pixels are grouped into clusters based on similarity. Each cluster is assigned random membership values, and the process continues iteratively until the desired membership degree is obtained. The pixel with the highest membership degree is ultimately chosen. Although the fast bilateral filter improves the image, some blurring and residual noise may persist. To address this, median and sharpening filters are applied, producing a noticeably enhanced final image.

3.2 *Utilizing a guide image for automatic parameter adjustment in the fast bilateral filter*

To address the challenge of selecting optimal parameters σ_r and σ_d in the fast bilateral filter, a guide image is employed to facilitate automatic parameter adjustment. Given the inherent complexity of medical images and the variability of noise patterns, manual tuning of these parameters is often inefficient and unreliable. Consequently, integrating a guide image into the filtering process has proven to be an effective strategy for enhancing parameter selection accuracy and improving the overall denoising performance.

The guide image acts as an auxiliary reference that informs the filter about the underlying structure and features present in the original image. By incorporating the guide image, the filter dynamically adapts its parameters based on the

intensity variations and spatial information shared between the original and guide images. This integration helps the filter preserve essential image details such as edges and textures while effectively suppressing noise.

In the fast bilateral filter, the guide image is integrated directly into the filtering process through a refined weighting mechanism. The mathematical formulation for incorporating the guide image into the fast bilateral filter is given by:

$$I_p^{bf} = \frac{\sum_{q \subset S} \sum_{\zeta \subset R} G_{\sigma_k}(|p-q|) \cdot G_{\sigma_r}(|i_p - \zeta|) \cdot \delta(\zeta - i_q) \cdot w_q \cdot i_q}{\sum_{q \subset S} \sum_{\zeta \subset R} G_{\sigma_k}(|p-q|) \cdot G_{\sigma_r}(|i_p - \zeta|) \cdot \delta(\zeta - i_q) \cdot w_q} \tag{6}$$

where:
- I_p^{bf} represents the filtered pixel intensity at position p.
- $G_{\sigma_k}(|p-q|)$ is the spatial Gaussian weight that controls the influence of neighboring pixels based on their spatial proximity.
- $G_{\sigma_r}(|i_p - \zeta|)$ is the feature space Gaussian weight, computed based on the intensity difference between the pixel value in the original image and the corresponding pixel value in the guide image.
- $\delta(\zeta - i_q)$ is the Kronecker delta function that ensures corresponding pixels between the original and guide images are appropriately aligned.
- w_q is a weighting factor for balancing contributions from different neighboring pixels.

1. Calculation of spatial weights:

For each pixel p in the image, spatial weights $G_{\sigma_k}(|p-q|)$ are calculated. These weights reflect the spatial distance between the current pixel p and its neighboring pixels q. The Gaussian function G_{σ_k} is employed to ensure that closer pixels exert stronger influence than those farther away. The parameter σ_k controls the rate at which spatial influence diminishes with distance.

2. Calculation of feature space weights:

For each pixel p, feature space weights $G_{\sigma_r}(|i_p - \zeta|)$ are computed based on the intensity difference between pixel p in the original image and the corresponding pixel ζ in the guide image. Here, i_p represents the pixel intensity at position p in the original image, and ζ represents the corresponding pixel intensity in the guide image. The parameter σ_r regulates the influence of intensity differences on the final filter output.

3. Calculation of the filtered image value:

The filtered image value I_p^{bf} is calculated as a weighted average of the pixel values in the guide image. This step combines the previously computed spatial and feature space weights along with the Kronecker delta function, ensuring alignment between corresponding pixels in the original and guide images. The weighted sum is normalized to maintain image intensity consistency.

3.2.1 *Advantages of using a guide image in the fast bilateral filter*

The integration of a guide image in the fast bilateral filter offers several key advantages:
- **Improved noise reduction:** The guide image provides additional structural information that helps the filter distinguish noise from meaningful image features, enhancing the overall noise suppression capability.
- **Enhanced detail preservation:** By utilizing the guide image, the filter more effectively retains crucial image details such as sharp edges and fine textures.
- **Automatic parameter adjustment:** The guide image assists in dynamically adjusting the filter's parameters, reducing the reliance on manual tuning and improving the filter's adaptability to diverse noise conditions.

In summary, incorporating a guide image in the fast bilateral filter effectively addresses the challenge of parameter selection, improving both the denoising performance and the preservation of vital image features. This technique significantly enhances the accuracy and reliability of medical image denoising applications.

3.3 *Incorporating spatial and local intensity information to enhance FCM performance*

In order to enhance the segmentation quality while reducing computational complexity, a fast bilateral filter is employed. The aim is to develop a method that integrates both the spatial positioning of pixels and their local intensity values to improve segmentation performance. By combining these factors, the improved objective function for the fuzzy C-means (FCM) algorithm is expressed as follows:

$$O_{\text{FCM}}^{(z)} = \sum_{i=1}^{K} \sum_{j=1}^{N} \left(u_{ij}^{(z)} \right)^m \| x_j - c_i^{(z)} \|^2 + \sum_{i=1}^{K} \sum_{j=1}^{N} \tag{7}$$

$$O_{\text{FCM}}^{(z)} = \sum_{i=1}^{K} \sum_{j=1}^{N} \alpha \left(u_{ij}^{(z)} \right)^m \| x_j - c_i^{(z)} \|^2 + \sum_{i=1}^{K} \sum_{j=1}^{N} \beta \left(u_{ij}^{(z)} \right)^m \| \bar{x}_j - c_i^{(z)} \|^2 \tag{8}$$

Here, the objective function $O_{\text{FCM}}^{(z)}$ introduces two key parameters, α and β, which govern the influence of the original image and the bilaterally filtered image in the segmentation process.

3.3.1 *Explanation of parameters*

• α (Alpha): This parameter controls the contribution of the original image to the segmentation outcome. A smaller α value indicates reduced influence from the original image, ensuring that segmentation results are less dependent on its details. Conversely, a larger α value strengthens the impact of the original image on segmentation.

• β (Beta): This parameter regulates the influence of the fast bilaterally filtered image. A larger β value increases the filtered image's role in segmentation, emphasizing noise reduction and improved feature consistency. Conversely, a smaller β value reduces the effect of the filtered image.

The parameters α and β are calculated as follows:

$$\beta = \left| x_j - \bar{x}_j \right| \tag{9}$$

$$\alpha = \frac{1}{\left| x_j - \bar{x}_j \right|} \tag{10}$$

where:
• x_j represents the pixel intensity value at location j in the original image.
• $\bar{x}_j$ represents the pixel intensity value at location j in the fast bilaterally filtered image.

3.3.2 *Explanation of parameters*

• α (Alpha): This parameter controls the contribution of the original image to the segmentation outcome. A smaller α value indicates reduced influence from the original image, ensuring that segmentation results are less dependent on its details. Conversely, a larger α value strengthens the impact of the original image on segmentation.

• β (Beta): This parameter regulates the influence of the fast bilaterally filtered image. A larger β value increases the filtered image's role in segmentation, emphasizing noise reduction and improved feature consistency. Conversely, a smaller β value reduces the effect of the filtered image.

The parameters α and β are calculated as follows.

3.3.3 *Interpretation and impact*

These definitions ensure that segmentation outcomes are more significantly influenced by the filtered image when β is larger and by the original image when α is smaller. Consequently, this strategy effectively balances the original image's details with the filtered image's improved noise suppression properties. The key advantage of this approach lies in its ability to dynamically adjust the influence of each image source, enabling more robust and accurate segmentation in medical images.

By integrating both spatial and local intensity information into the FCM framework, this enhanced method achieves improved noise resilience and segmentation precision, particularly in complex medical imaging scenarios where detail preservation is crucial.

3.4 *Use of hybrid membership*

In FCM, we use the Lagrange multiplier method to extract the formulae for membership degree and clustering center update in order to minimize the objective function, which can be realized after all. For fewer steps, we use the sum of membership degrees calculated in the earlier iterations, referred to as membership links:

$$L = \ln^2 \left(\sum_{f=1}^{N} u_{if}^{(z-1)} + 1 \right) \tag{11}$$

And the membership function is finally completed in this step objective function is:

$$O_{FCm}^{(z)} = \sum_{i=1}^{K} \frac{\sum_{j=1}^{N} \alpha \left(u_{ij}^{(z)} \right)^m \parallel x_j - c_i^{(z)} \parallel^2 + \sum_{j=1}^{N} \beta \left(u_{ij}^{(z)} \right)^m \parallel \bar{x}_j - c_i^{(z)} \parallel^2}{\ln^2 \left(\sum_{f=1}^{N} u_{if}^{(z-1)} + 1 \right)}, \quad \sum_{i=1}^{K} u_{ij}^{(z)} = 1 \tag{12}$$

where $u_{ij}^{(z)}$ is fuzzy factor j in cluster i during the iteration.

To establish this relationship, we initially employ the Lagrange multiplier method to incorporate the constraint of probability summation. Subsequently, we demonstrate this relationship by optimizing the objective equation using the technique of variable separation and internal variables.

We utilize the Lagrange theorem to solve the following optimization problem:

$$L \left(u_{ij}^{(z)}, \lambda \right) = \sum_{i=1}^{K} \sum_{j=1}^{N} \left[\alpha \left(u_{ij}^{(z)} \right)^m \parallel x_j - c_i^{(z)} \parallel^2 + \beta \left(u_{ij}^{(z)} \right)^m \parallel \bar{x}_j - c_i^{(z)} \parallel^2 \right]$$

$$+ \lambda \left(\sum_{f=1}^{N} u_{if}^{(z)} - 1 \right) \tag{13}$$

where λ represents the Lagrange multiplier.

To determine the minimum of the objective function, we set the partial derivatives with respect to $u_{ij}^{(z)}$ to zero and the partial derivative with respect to λ equal to zero.

For the partial derivative with respect to $u_{ij}^{(z)}$:

$$\frac{\partial L}{\partial u_{ij}^{(z)}} = m\alpha \left(u_{ij}^{(z)}\right)^{m-1} \left(\|x_j - c_i^{(z)}\|^2 + \frac{\beta\left(u_{ij}^{(z)}\right)}{\alpha\left(u_{ij}^{(z)}\right)} \|\bar{x}_j - c_i^{(z)}\|^2 \right) + \lambda = 0 \tag{14}$$

Now, we add this equation to our original equation:

$$m\alpha \left(u_{ij}^{(z)}\right)^{m-1} \left(\|x_j - c_i^{(z)}\|^2 + \frac{\beta\left(u_{ij}^{(z)}\right)}{\alpha\left(u_{ij}^{(z)}\right)} \|\bar{x}_j - c_i^{(z)}\|^2 \right) + \lambda = 0 \tag{15}$$

$$\alpha \left(u_{ij}^{(z)}\right)^{m-1} \left(\|x_j - c_i^{(z)}\|^2 + \frac{\beta\left(u_{ij}^{(z)}\right)}{\alpha\left(u_{ij}^{(z)}\right)} \|\bar{x}_j - c_i^{(z)}\|^2 \right) + \frac{\lambda}{m} = 0 \tag{16}$$

$$\alpha \left(u_{ij}^{(z)}\right)^{m-1} \left(\|x_j - c_i^{(z)}\|^2 + \frac{\beta\left(u_{ij}^{(z)}\right)}{\alpha\left(u_{ij}^{(z)}\right)} \|\bar{x}_j - c_i^{(z)}\|^2 \right) = -\frac{\lambda}{m} \tag{17}$$

$$\alpha \left(u_{ij}^{(z)}\right)^{m-1} = -\frac{\lambda}{m} \left(\|x_j - c_i^{(z)}\|^2 + \frac{\beta\left(u_{ij}^{(z)}\right)}{\alpha\left(u_{ij}^{(z)}\right)} \|\bar{x}_j - c_i^{(z)}\|^2 \right)^{-1} \tag{18}$$

By substituting $\alpha\left(u_{ij}^{(z)}\right)$ from Equation (2) (the probability equation), we have:

$$\alpha \left(u_{ij}^{(z)}\right) = \left(\frac{\lambda}{m} \left(\|x_j - c_i^{(z)}\|^2 + \frac{\beta\left(u_{ij}^{(z)}\right)}{\alpha\left(u_{ij}^{(z)}\right)} \|\bar{x}_j - c_i^{(z)}\|^2 \right)^{-1} \right)^{\frac{1}{m-1}} \tag{19}$$

Now, by substituting the value of $\alpha\left(u_{ij}^{(z)}\right)$ into the original objective function, the objective equation for optimal values of $u_{ij}^{(z)}$ will be:

$$\sum_{i=1}^{K}\sum_{j=1}^{N} \left[\left(\frac{\lambda}{m} \left(\|x_j - c_i^{(z)}\|^2 + \frac{\beta\left(u_{ij}^{(z)}\right)}{\alpha\left(u_{ij}^{(z)}\right)} \|\bar{x}_j - c_i^{(z)}\|^2 \right)^{-1} \right)^{\frac{m}{m-1}} \|x_j - c_i^{(z)}\|^2 + \beta\left(u_{ij}^{(z)}\right) \|\bar{x}_j - c_i^{(z)}\|^2 \right] \tag{20}$$

with the Lagrange theorem and the constraint of summing probabilities, we compute the optimal values of $u_{ij}^{(z)}$.

In other papers presented to improve fuzzy clustering in order to remove noise [5, 22, 50], a maximum of two noises are combined to test images. In the proposed method, mixed noise is added to all examined images to experiment on the methods. It is generated using four types of noise here.

3.5 *Combining median filtering and sharpening is a beneficial approach to enhance image clarity while preserving details*

Addressing issues from the fast bilateral filter, this method utilizes sharpening to improve detail clarity and then applies median filtering to remove noise while retaining image details, resulting in improved image quality.

3.5.1 *The sharpening filter*

It commonly used in image processing, aims to enhance image details and edges, thereby improving overall clarity. One popular sharpening filter is the Laplacian filter, which enhances contrast between adjacent pixels, emphasizing edges or rapid intensity changes within the image. Mathematically, the Laplacian filter is defined as:

$$\text{Laplacian}(x, y) = \frac{\partial^2 I}{\partial x^2} + \frac{\partial^2 I}{\partial y^2} \tag{21}$$

Based on the Equation (21): Here, I represents the input image, and $\frac{\partial^2 I}{\partial x^2}$ and $\frac{\partial^2 I}{\partial y^2}$ denote the second-order derivatives of the image with respect to the x and y coordinates, respectively. The Laplacian filter enhances the image's ability to detect edges and fine details, resulting in a sharper appearance.

3.5.2 *The median filter*

It is widely used for noise removal and image enhancement. It calculates the median value of pixel intensities within a specified neighborhood, effectively removing noise such as salt-and-pepper noise and Gaussian noise.

The Median filter selects a neighborhood for each pixel in the image, sorts pixel values in nondescending order, and calculates the median value. This median value replaces the original pixel value, providing resistance against outliers in the image. The formula for calculating the pixel value using the Median filter is:

$$I_{\text{filtered}}(x, y) = \text{Median}\{I(x+i, y+j) \mid i, j \in [-a, a]\} \tag{22}$$

Based on the Equation (22): Here, $I_{\text{filtered}}(x, y)$ represents the new pixel value for the target pixel, $I(x+i, y+j)$ denotes the pixel values of neighboring pixels in the input image matrix, and a specifies the size of the neighborhood used for median value calculiion.

4. Experimental results

In this section, the proposed method is analyzed. First, the evaluation indicators and parameters are introduced. Then, the results of the experiments are discussed, and comparisons are made to similar methods.

4.1 *Datasets*

This study utilizes two essential datasets. The first is the structural MRI dataset, which includes T1, T2, and FLAIR images. These images are prepared with key preprocessing steps, such as inhomogeneity correction and brain extraction, making them a valuable resource for evaluating noise reduction algorithms and image processing techniques.

The second dataset, "Low Dose CT Image and Projection Data", contains both regular clinical dose CT images and simulated lower dose CT images, specifically designed for cancer studies. This dataset aids researchers in assessing and improving image processing methods.

The download links for these datasets are as follows:
- Structural MRI dataset: https://www.kaggle.com/datasets/ilknuricke/neurohackinginrimages.
- Low Dose CT dataset: www.cancerimagingarchive.net.

4.2 *Evaluation criteria*

To evaluate the proposed method for addressing noisy images, several criteria are defined:

- **Segmentation accuracy (SA):** This is the ratio of the total number of correctly clustered pixels to the total number of pixels. It provides a measure of how well the image has been segmented compared to the ground truth.

- **Mean intersection over union (mI):** This metric is calculated similarly to SA, where the segmented image is compared to the ground truth. Higher values of mI indicate better segmentation.

- **Recall:** This metric quantifies the ability of the method to detect all relevant pixels. A larger number of incorrect detections lowers recall.

- **Precision:** This metric evaluates the accuracy of the detections. The larger the number of unpredicted items, the lower the precision.

- **F1-Score:** This is the harmonic mean of recall and precision, offering a balance between the two metrics. The geometric mean of the F1-score and the **E-Measure** is used to assess the overall performance of the segmentation.

- **Peak signal-to-noise ratio (PSNR):** This metric evaluates the quality of the denoised image by comparing the peak signal with the noise.

- **Structural similarity index (SSIM):** SSIM measures the similarity between the denoised image and the ground truth image in terms of luminance, contrast, and structure.

- **Mean squared error (MSE):** Recently added to the evaluation criteria, MSE helps assess the difference between the predicted and true images. A lower MSE indicates better performance.

According to the above definition of segmentation accuracy,

$$\text{SA} = \frac{\sum_{i=1}^{K} B_i \cap C_i}{\sum_{j=1}^{K} C_j} \tag{23}$$

Based on the Equation (23), where B_i is the set of pixels available in cluster i that are obtained using this method, and C_i is the set of pixels available in the clusters located in the ground. A larger value of SA denotes a better result. The mean intersection over union is defined as follows:

$$\text{MI} = \frac{1}{K} \sum_{i=1}^{K} \frac{B_i \cap C_i}{B_i \cup C_i} \tag{24}$$

Based on the Equation (24), where all the symbols are the same as those in SA, indicating that the segmented image is equal to the ground truth. A larger value of mIdenotes a better result. E-Measure is defined as follows:

$$\text{E-Measure} = \frac{1}{4mn} \sum_{x=1}^{m} \sum_{y=1}^{n} \left\{ 1 + \frac{2 \left[I_{GT}(x, y) - \mu_{GT} \right] \left[I_{FM}(x, y) - \mu_{FM} \right]}{\left[I_{GT}(x, y) - \mu_{GT} \right]^2 + \left[I_{FM}(x, y) - \mu_{FM} \right]^2} \right\}^2 \tag{25}$$

Based on the Equation (25), where m and n are image length and width, respectively. $I_{GT}(x, y)$ and $I_{FM}(x, y)$ represent the brightness of the pixels located at x, y in the ground truth and in the segmented result, correspondingly. μ_{GT} and μ_{FM} indicate the global value and the segmented result, respectively. A larger value of E-Measure denotes a better result.

Peak signal-to-noise ratio (PSNR): PSNR is a well-known metric used to evaluate the quality of a reconstructed image compared to its original version. It calculates the ratio between the maximum possible signal power (original image) and the noise power (difference between the original and denoised images). Measured in decibels (dB), higher PSNR values indicate superior image quality and more effective noise reduction. In medical imaging, PSNR values above 30 dB are generally considered satisfactory. This metric plays a key role in assessing the performance of denoising algorithms.

Structural similarity index (SSIM): SSIM is a perceptual metric designed to measure the similarity between two images by analyzing structural information, luminance, and contrast. Unlike PSNR, which focuses on pixel-wise differences, SSIM reflects the human visual system's sensitivity to structural details. SSIM values range from -1 to 1, with values closer to 1 indicating higher similarity and better preservation of the original image's features. This makes SSIM a valuable tool for evaluating the visual quality of denoised images.

Mean squared error (MSE): It is a widely recognized metric for assessing the accuracy of reconstructed images compared to reference images. This metric measures the average squared difference in pixel intensities between two images and is mathematically defined as:

$$MSE = \frac{1}{MN} \sum_{i=1}^{M} \sum_{j=1}^{N} (I(i, j) - K(i, j))^2 \tag{26}$$

where:
- $I(i, j)$ represents the pixel intensity at position (i, j) in the reference image.
- $K(i, j)$ represents the corresponding pixel intensity in the reconstructed image.
- M and N denote the number of rows and columns in the image, respectively.

A lower MSE value indicates greater similarity between the reference and reconstructed images, reflecting higher reconstruction quality. Conversely, a higher MSE value suggests greater differences and poorer quality. An MSE value of zero signifies perfect alignment between the two images. Due to its simplicity and effectiveness, MSE remains a fundamental metric for evaluating image accuracy across a broad range of applications.
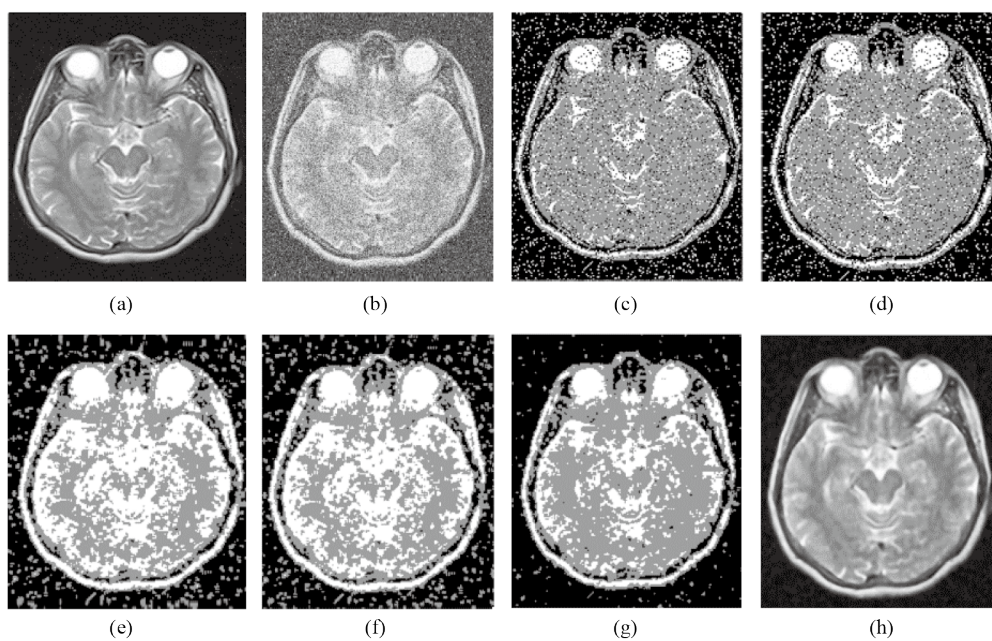
4.3 Results

This section presents the experimental results of the proposed IFCM-DMF method, which were conducted using real medical images, including CT1, CT4, CT5, T1, and T2. The results obtained from this method are compared with those from the algorithms FCM, IFCM, AFC-PFS, AIPFCM, and APFCM-S (refer to Section 2 and Table 2). Figures 4 and 5 illustrate the performance of the IFCM-DMF method under conditions where combined noise is applied to the input image. Figure 4a displays the original CT1 image, while Figure 4b depicts an image with combined noise. The results obtained from various algorithms are presented in Figure 4c and h, with Figure 4h specifically highlighting the superior performance of the IFCM-DMF method compared to other algorithms. This superiority arises from the method's effectiveness in managing combined noise scenarios and utilizing dynamic membership functions.

While all methods aim to reduce noise, it is evident that the IFCM-DMF method achieves the highest PSNR and SSIM values. These results demonstrate the method's superior ability to preserve image quality and details compared to other approaches, establishing it as an efficient and effective technique for noise reduction in medical images.
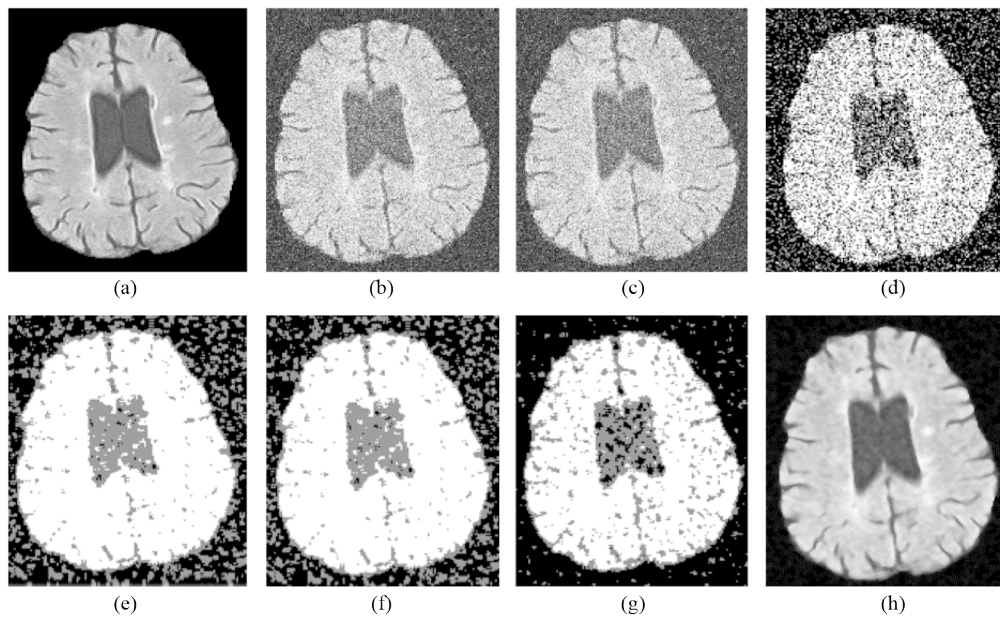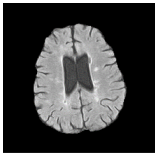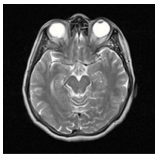
Figure 4. Comparison of results on a CT1 image corrupted by noise: (a) Original image; (b) Noisy image; (c) FCM; (d) IFCM; (e) AFC-PFS; (f) AIPFCM; (g) APFCM-S; (h) IFCM-DMF (proposed method)
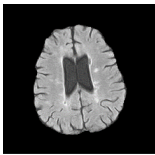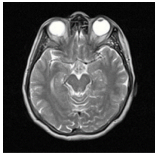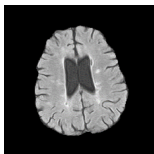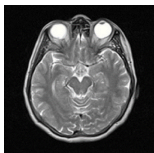

Figure 5. Comparison of results on a CT4 image corrupted by noise: (a) Original image; (b) Noisy image; (c) FCM; (d) IFCM; (e) AFC-PFS; (f) AIPFCM; (g) APFCM-S; (h) IFCM-DMF (proposed method)

Table 3. Comparison of different algorithms based on SA (%)

SA (%) comparisons of six methods	density	FCM	IIFCM	AFC-PFS	AIPFCM	APFCM-S	IFCM-DMF
	0.05	96.29	95.32	96.76	95.08	**97.74**	97.51
	0.1	78.61	86.05	86.05	91.93	95.69	**97.28**
	0.15	68.95	76.38	76.38	87.73	92.77	**97.12**
	0.2	60.2	73.92	73.92	81.44	85.49	**96.47**
	0.05	94.75	95.41	95.08	**98.72**	97.75	98.27
	0.1	59.32	92.8	91.58	93.62	**94.89**	97.65
	0.15	45.73	73.38	81.84	89.44	89.78	**94.21**
	0.2	57.33	66.27	66.27	80.7	81.76	**94.17**

Table 4. Comparison of different algorithms based on mI (%)

mI (%) comparisons of six methods	density	FCM	IIFCM	AFC-PFS	AIPFCM	APFCM-S	IFCM-DMF
	0.05	92.48	91.11	95.5	**96.66**	94.83	96.25
	0.1	64.28	89.58	91.29	86.49	73.86	**94.56**
	0.15	52.33	85.54	85.76	86.49	73.86	**91.31**
	0.2	46.47	79.22	73.85	52.68	61.34	**90.32**
	0.05	73.86	90.15	95.37	90.58	94.75	**96.85**
	0.1	61.34	90.15	69.55	74.96	91.5	**93.25**
	0.15	54.15	84.32	69.55	74.96	91.5	**91.83**
	0.2	48.25	77.22	55.3	61.66	87.43	**89.33**

Table 5. Comparison of different algorithms based on E-Measure (%)

| E-Measure (%) comparisons of six methods	Density	FCM	IIFCM	AFC-PFS	AIPFCM	APFCM-S	IFCM-DMF
	0.05	96.25	95.57	97.82	**98.04**	97.50	98.36
	0.10	76.97	94.78	95.71	93.12	85.77	**98.52**
	0.15	66.25	92.52	92.78	60.00	77.35	**98.44**
	0.20	60.12	88.63	85.19	43.99	71.26	**98.00**
	0.05	96.81	97.75	95.76	97.31	96.38	**99.21**
	0.10	95.08	80.75	93.6	92.18	95.12	**98.01**
	0.15	91.96	68.32	89.66	75.83	93.71	**97.37**
	0.20	87.72	60.58	83.74	63.60	91.60	**96.98**

Comparisons in Tables 2-4 show that the proposed method outperforms from other methods in different measures.

Furthermore, Table 5 presents the PSNR and SSIM and values for each method, serving as key indicators for evaluating image quality and detail preservation.
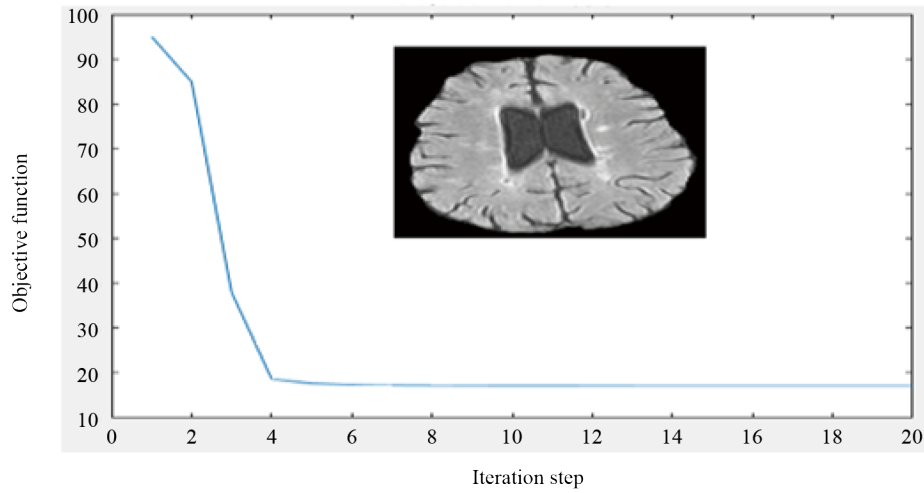
**Figure 6.** Objective function curves that normalized into [0, 1]

Figures 6 and 7 illustrate the objective function curves of the CT1 and CT4 images. As depicted in the figures, it can be observed that the image has achieved the desired state after four or more iterations.
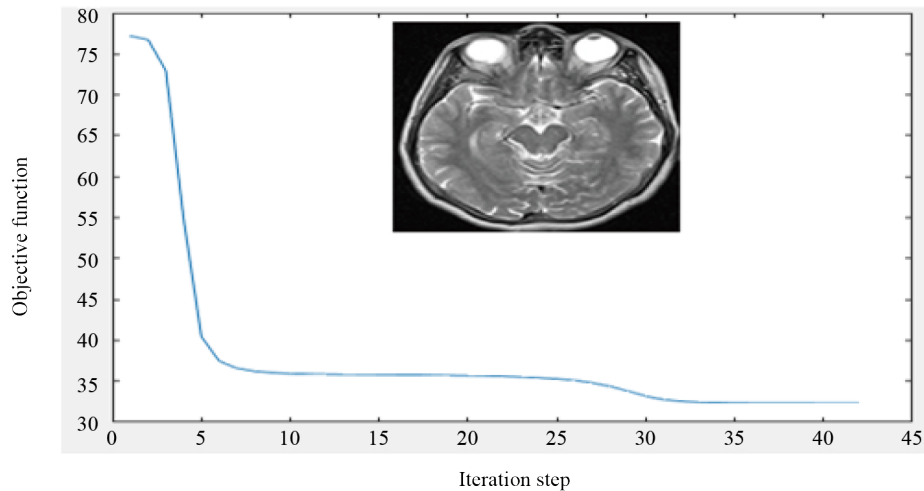

Figure 7. Objective function curves that normalized into [0, 1]

Figures 8 and 9 present a separate and additive comparison of T1/T2 images using various brain images. The proposed method has demonstrated excellent performance in effectively handling the mixture of different types of noise.
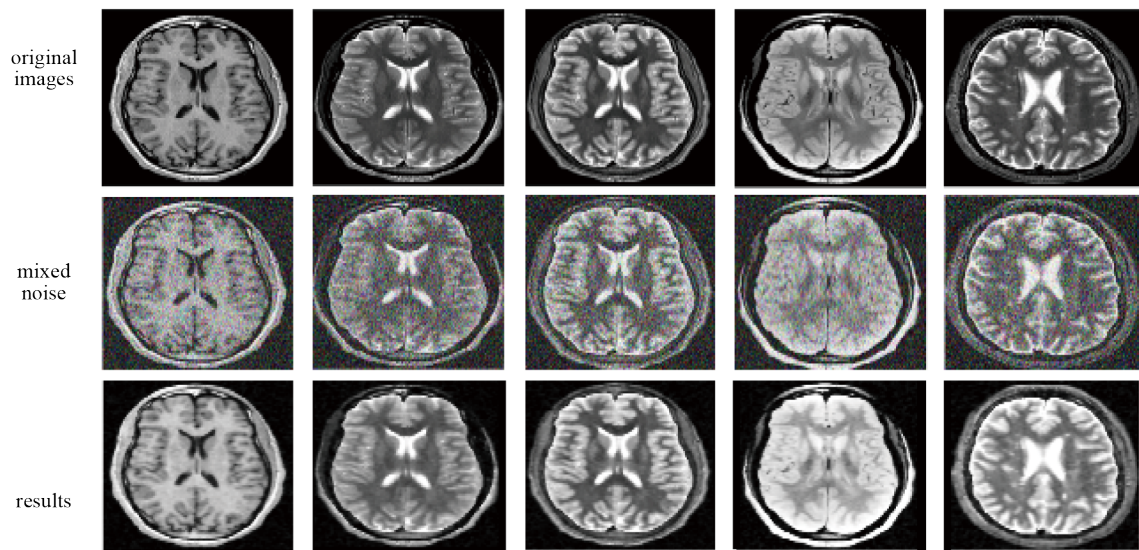
Figure 8. Comparison of results obtained by IFCM-DMF (proposed method) on a T1/T2 image corrupts by mixed noise
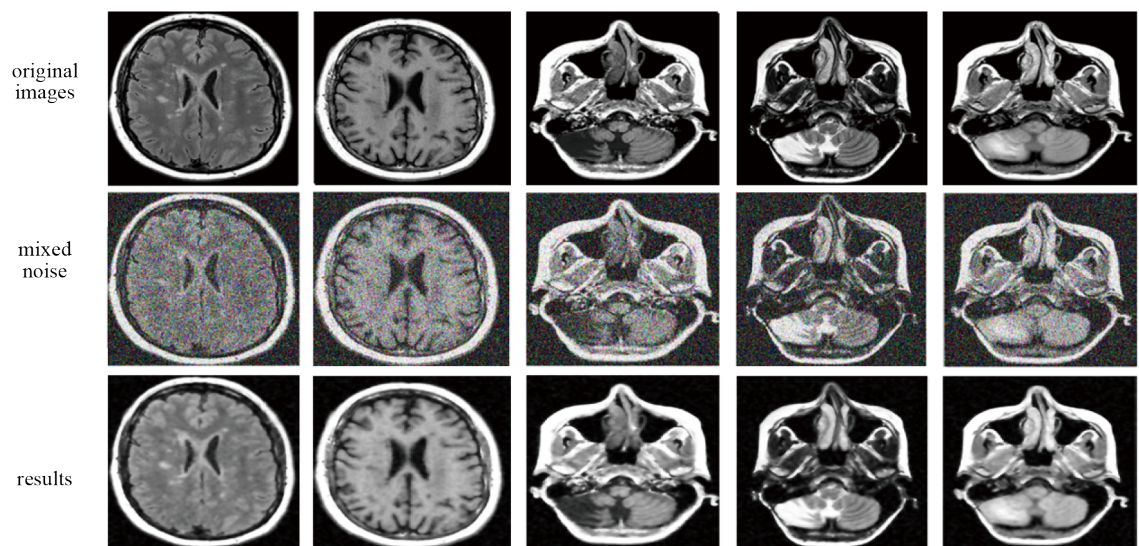

Figure 9. Comparison of results obtained by IFCM-DMF (proposed method) on a T1/T2 image corrupts by mixed noise

Figures 10-12 present the performance evaluation of the proposed methods when subjected to combined noise applied to the input image. In images (a, d), the original image is displayed, while image (b) exhibits mixed noise with a lower intensity, and image (e) showcases mixed noise with increasing intensity. Image (c) illustrates the results obtained from the algorithms described in articles [7, 12]. It is evident that the noise in the images persists to some extent, resulting in blurred images with limited visibility of fine details. Image (f) demonstrates the superior performance of the proposed method in dealing with higher noise intensities, as it effectively removes noise and enhances segmentation compared to other algorithms. This improved performance can be attributed to the stability of the proposed method, achieved through the utilization of dynamic membership functions in the mode of combining different types of noise.
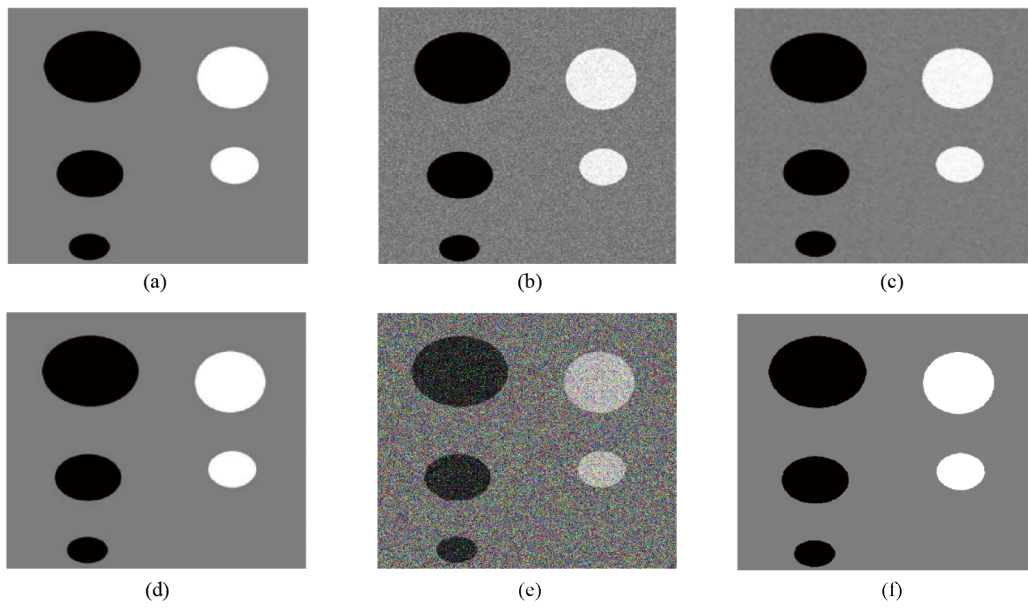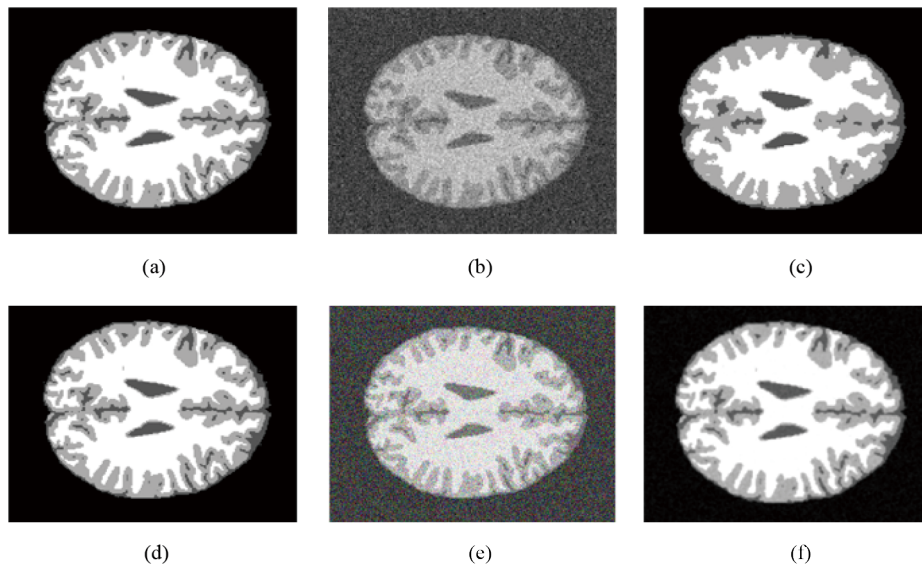
Figure 10. (a, d) Original image; (b, e) Noisy image; (c) medical X-ray images; (f) IFCM-DMF (proposed method)
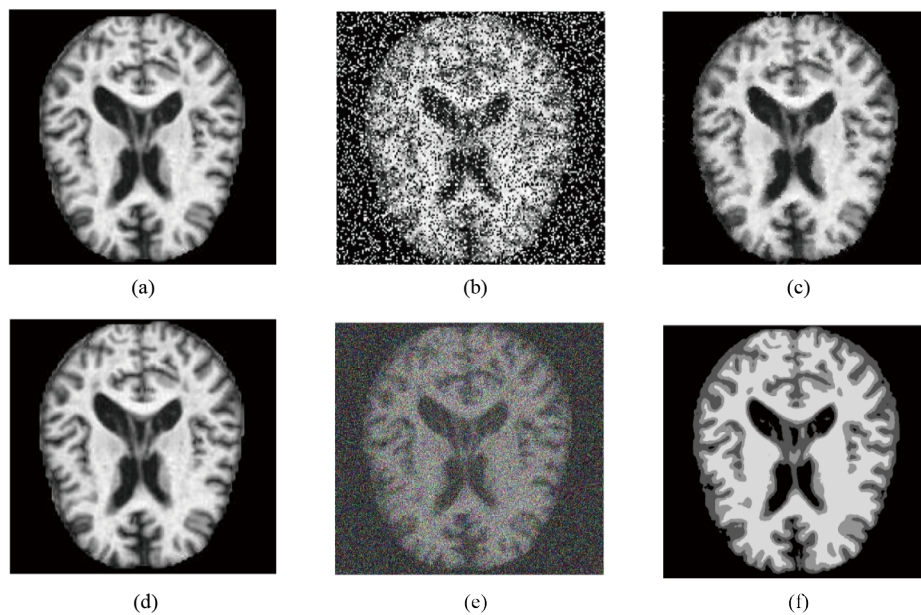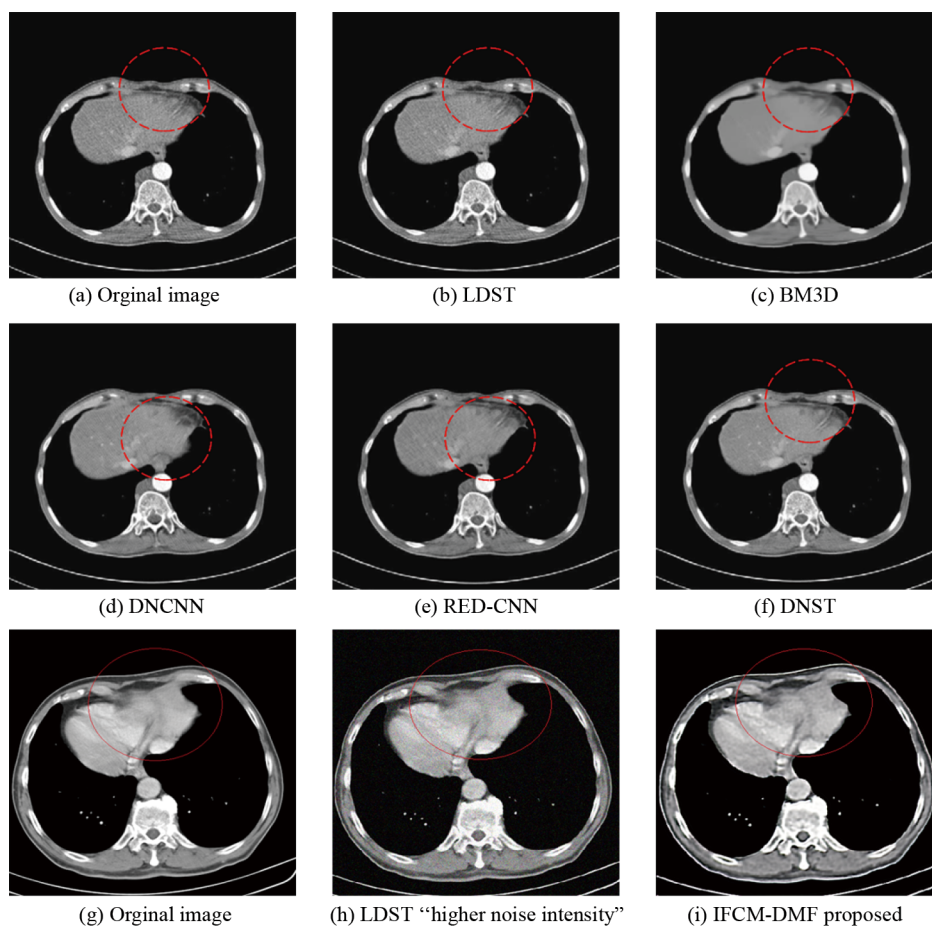

Figure 11. (a, d) Original image; (b, e) Noisy image; (c) FPAENH; (f) IFCM-DMF (proposed method)

In comparison to the aforementioned methods, the proposed approach incorporates a fast bilateral filter and adaptive weights that not only consider spatial and intensity information but also leverage the original FCM. This combination allows for effective reduction of noise pixels in the resulting images, surpassing the performance of the previously mentioned methods.

Figure 12. (a, d) Original image; (b, e) Noisy image; (c) $GCFE_s$; (f) IFCM-DMF (proposed method)

(a) Orginal image

(b) LDST

(c) BM3D

(d) DNCNN

(e) RED-CNN

(f) DNST

(g) Orginal image

(h) LDST ''higher noise intensity''

(i) IFCM-DMF proposed

Figure 13. Comparison of methods: DnCNN-CT, RED-CNN, DnST, and the proposed IFCM-DMF method

Figure 13 provides a comparison between the methods DnCNN-CT, RED-CNN, DnST, and the proposed IFCM-DMF method. The IFCM-DMF method effectively reduces noise and enhances image quality while preserving crucial details. The regions highlighted with red circles contain more complex details, showcasing the IFCM-DMF's capability to maintain fine details and recover important textures that may be lost with other methods.

The proposed IFCM-DMF method presents an optimized solution for medical image denoising, aimed at enhancing image quality while preserving critical details. In comparison with other methods such as DnCNN-CT, RED-CNN, and DnST, IFCM-DMF demonstrates superior performance, particularly in recovering fine details in low-dose images. The regions marked by red circles, which contain more intricate details, were selected for a more precise evaluation. These highlighted areas showcase IFCM-DMF's ability to retain fine details and restore important textures, which may be lost with other methods. IFCM-DMF not only effectively reduces noise, but also enhances image clarity and precision, especially in sensitive and detailed regions. These results affirm the superiority of the proposed method in improving the quality of medical images, positioning it as an efficient and effective approach for noise reduction.

Table 6 presents the PSNR and SSIM metrics for each method, which serve as key indicators for evaluating image quality and detail preservation. While all methods aim to reduce noise, it is clear that the IFCM-DMF method achieves the highest PSNR and SSIM values. This demonstrates the method's superior ability to maintain image quality and preserve details compared to the other approaches.

**Table 6.** Comparison of methods based on PSNR and SSIM

Comparison of methods based on PSNR and SSIM	Methods	PSNR	SSIM
	LDCT	32.385	0.912
	BM3D	30.916	0.913
	DnCNN-CT	33.515	0.922
	RED-CNN	33.352	0.913
	DnST	35.198	0.937
	IFCM-DMF	**36.160**	**0.940**

Figure 14 presents a comparison between the proposed method and various advanced denoising techniques for MRI images, including ONLM [51], AONLM [52], PRINLM [53], MRNLM [54], CURE-Let [55], RiceVST [56], UKR [57], RRD [58], DnCNN [59], RED-WGAN [60], DABN [61], RIRGAN [62], and VDL-MRI [37]. This comparison is conducted on the Axial T1 image with Rician noise at a level of 0.06.
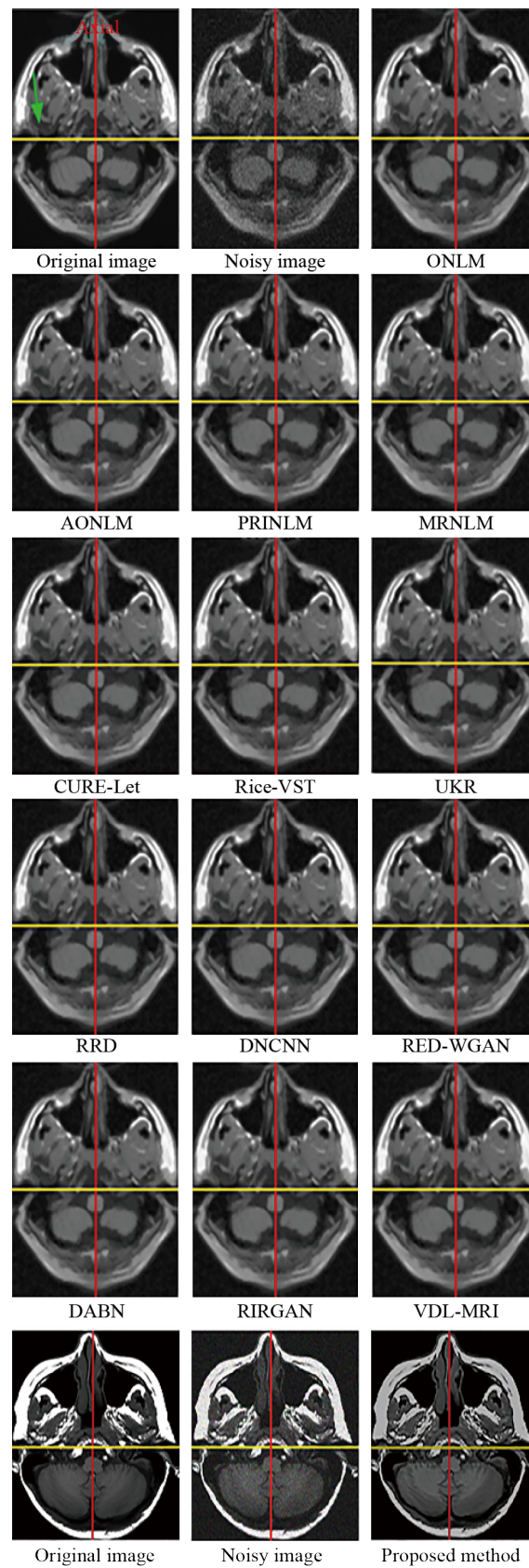
Figure 14. Presents a comparison of the proposed method with other techniques applied to the Axial T1 image with Rician noise of 0.06
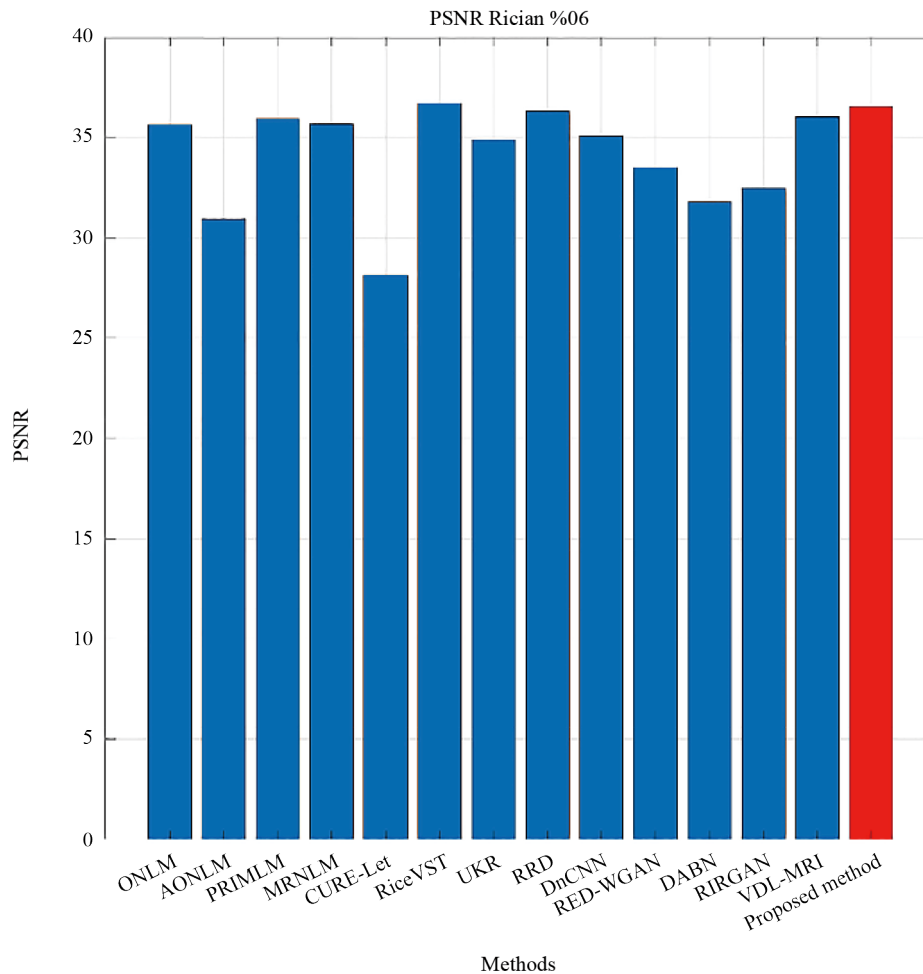
Figure 15. PSNR for the axial T1 image

Rician noise is a common type of noise in medical images, especially in MRI scans. This noise arises due to the nature of MRI imaging, involving a combination of Gaussian noise in the real and imaginary components of the signal. Rician noise has a greater impact in regions with lower signal intensities, leading to a reduction in contrast and loss of image details. This characteristic makes Rician noise particularly challenging to remove in medical image processing, as conventional denoising methods may degrade crucial image structures.

The results presented in Figure 14 clearly show that the proposed method outperforms the others in denoising while preserving fine image details. Unlike many other methods that may lead to loss of detail or the introduction of artifacts, our approach effectively reduces noise and significantly enhances the image's clarity and sharpness, demonstrating its superiority over existing techniques.

Figure 15 illustrates the peak signal-to-noise ratio (PSNR) values for the Axial T1 image, assessing the overall denoising performance of the proposed method. PSNR measures the ratio between the maximum possible signal power and the noise level in the image, with higher values indicating better noise reduction. The comparison with existing techniques highlights the superior ability of the proposed method to suppress noise while maintaining image quality.

Figure 16 shows the structural similarity index (SSIM) values for the Axial T1 image, evaluating how well the proposed method preserves structural details compared to other denoising techniques. SSIM is a critical metric for assessing the perceptual similarity between the original and denoised images, focusing on structural integrity and feature preservation. The results indicate that the proposed method maintains essential image details while effectively reducing

noise, outperforming both conventional and deep learning-based methods such as ONLM, AONLM, PRINLM, MRNLM, CURE-Let, RiceVST, UKR, RRD, DnCNN, RED-WGAN, DABN, RIRGAN, and VDL-MRI.
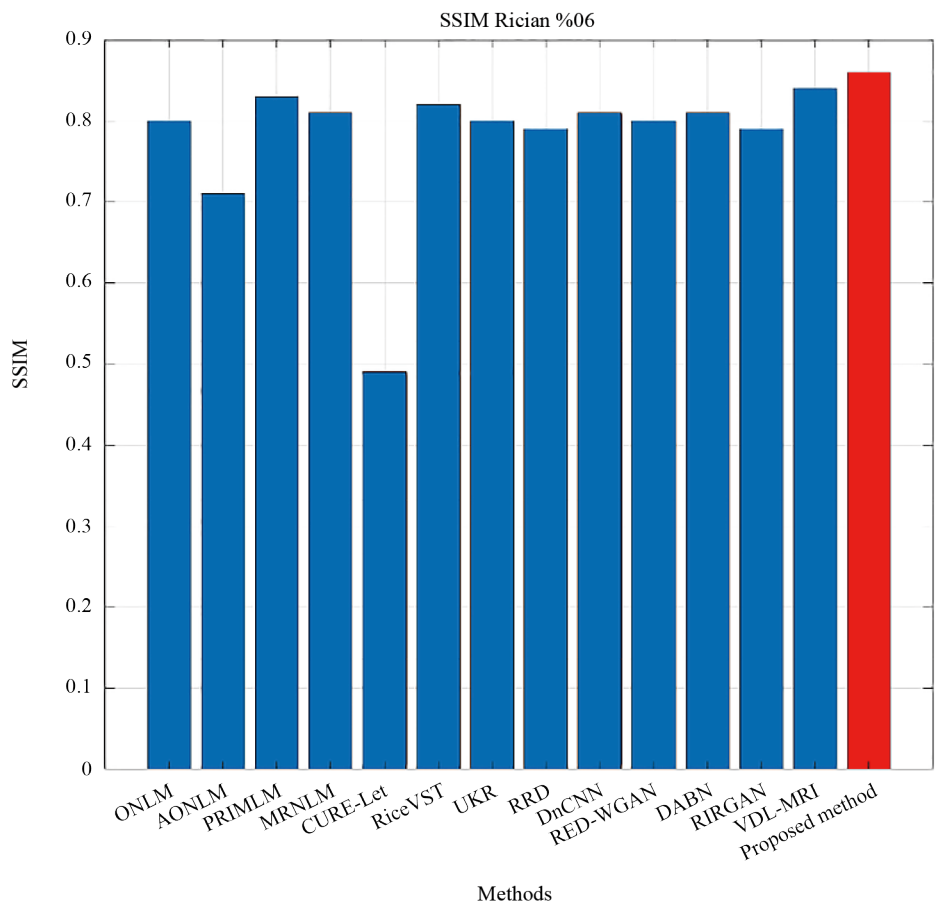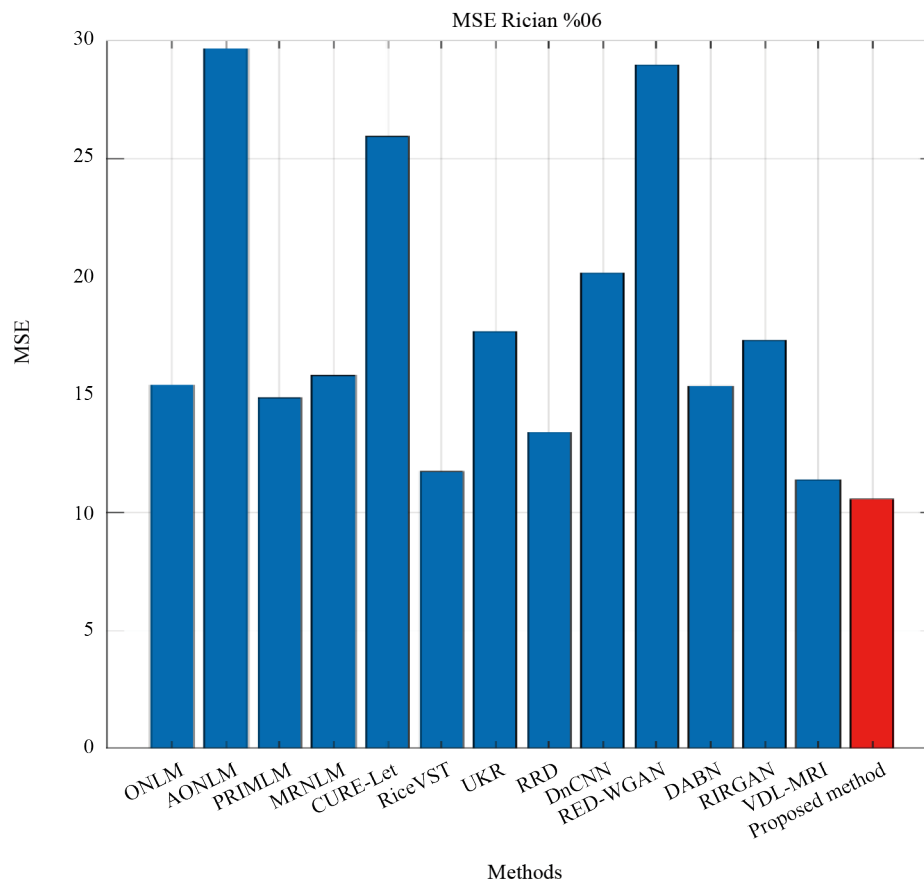

Figure 16. SSIM for the axial T1

Figure 17 presents the mean squared error (MSE) values for the Axial T1 image, quantifying the average squared differences between the original and denoised images. Lower MSE values indicate better noise suppression and higher reconstruction accuracy. The results show that the proposed method achieves significantly lower MSE compared to ONLM, AONLM, PRINLM, MRNLM, CURE-Let, RiceVST, UKR, RRD, DnCNN, RED-WGAN, DABN, RIRGAN, and VDL-MRI. This underscores the effectiveness of the proposed approach in reducing noise while maintaining the fidelity of medical images.

Table 7 presents the evaluation results of various denoising methods for Axial T1 images based on the PSNR, SSIM, and MSE metrics. The methods compared in this table include ONLM [51], AONLM [52], PRINLM [53], MRNLM [54], CURE-Let [55], RiceVST [56], UKR [57], RRD [58], DnCNN [59], RED-WGAN [60], DABN [61], RIRGAN [62], and VDL-MRI [37].

Figure 17. MSE for the axial T1 image

Table 7. Axial T1

Methods	PSNR	SSIM	MSE
ONLM [51]	35.65	0.80	15.4199
AONLM [52]	30.96	0.71	29.6538
PRINLM [53]	35.95	0.83	14.8621
MRNLM [54]	35.69	0.81	15.8154
CURE-Let [55]	28.14	0.49	25.9466
RiceVST [56]	36.72	0.82	11.7241
UKR [57]	34.9	0.80	17.6636
RRD [58]	36.33	0.79	13.3992
DnCNN [59]	35.09	0.81	20.1410
RED-WGAN [60]	33.51	0.80	28.9788
DABN [61]	31.81	0.81	15.3490
RIRGAN [62]	32.48	0.79	17.3014
VDL-MRI [37]	36.02	0.84	11.3784
Proposed method	36.56	0.86	10.5701
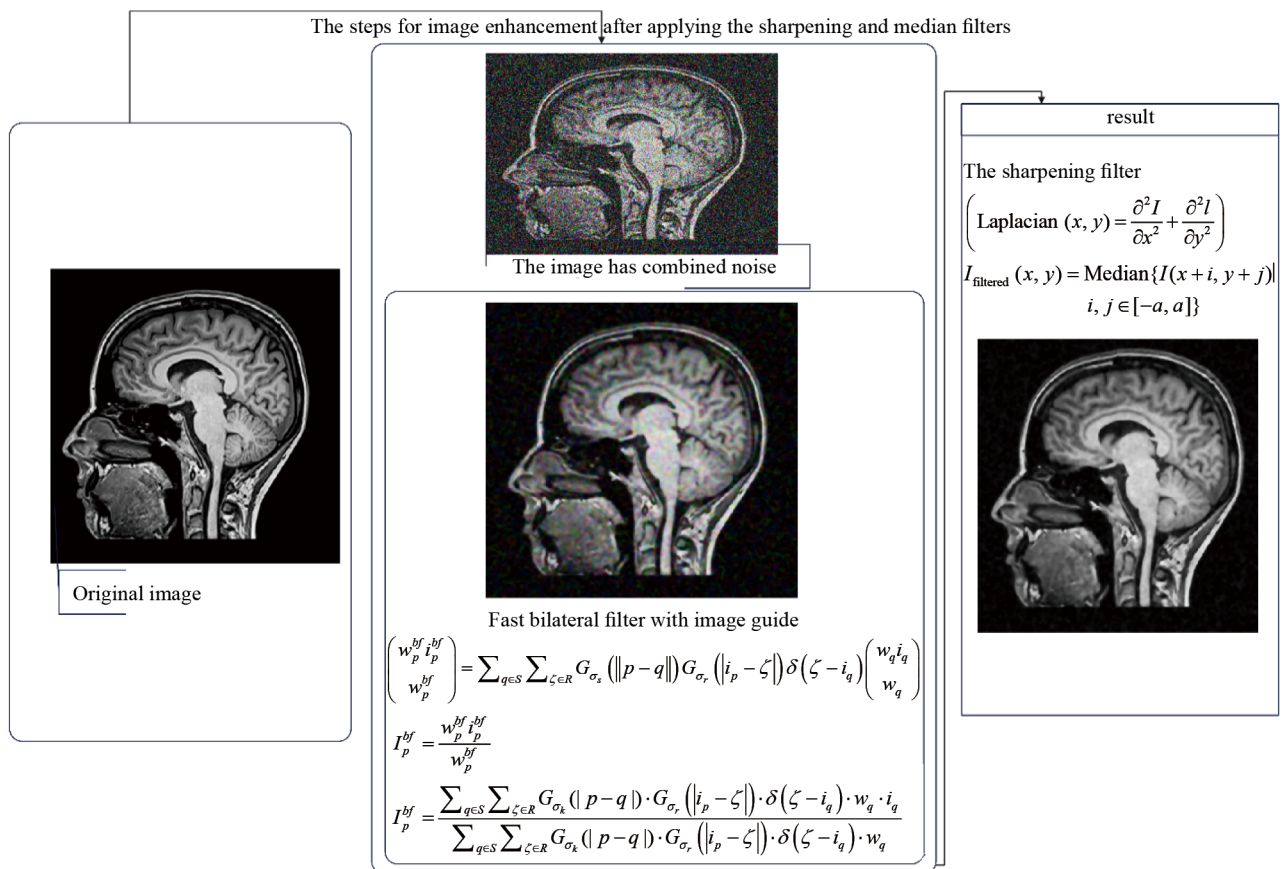
Figure 18. The result of applying sharpening and median filters to the image, and the final improvement of the image

Figure 18 presentsresult of applying sharpening and median filters to the image, and the final improvement of the image. In this methodology, the original image, post-initial parameter adjustments and the introduction of mixed noise, undergoes noise reduction via a fast bilateral filter employing a reference image. However, as the resulting image from the fast bilateral filter still retains noise and blurring, significant noise reduction is accomplished in the final stage through the application of median and sharpening filters.

5. Conclusions and future directions

The rapid advancement of digital systems in medical diagnostics has intensified the demand for robust image processing techniques capable of effectively suppressing noise without compromising crucial image details. Since noise in medical images can significantly degrade diagnostic accuracy, developing advanced denoising approaches that maintain key features such as edges and textures is paramount.

This study introduces an enhanced fuzzy clustering method that delivers substantial improvements in medical image denoising through the following key innovations:

1. **Superior local feature preservation:** By incorporating local intensity and spatial information alongside a fast bilateral filter, the proposed method strikes an optimal balance between computational efficiency and high-quality noise reduction.

2. **Refined clustering precision:** The integration of noise-adaptive constraints and enhanced image difference calculations ensures improved clustering accuracy, enabling precise noise suppression while preserving vital image structures.

3. **Accelerated iterative processing:** Leveraging cumulative membership information from previous iterations significantly reduces the required number of iterations, enhancing computational efficiency without compromising denoising performance.

Empirical results demonstrate the method's clear superiority over conventional techniques, achieving remarkable gains in noise reduction, computational efficiency, and overall performance. This enhanced framework holds strong potential to become a powerful tool for improving medical image quality in real-world clinical settings.

Future directions

While the proposed method has demonstrated robust performance, several important research avenues warrant further investigation:

1. **Expanding applicability:** Future studies should assess the method's effectiveness across diverse imaging modalities, including MRI, CT, and ultrasound, to ensure consistent performance in varied clinical scenarios. Additionally, evaluating its scalability for high-resolution datasets is crucial to accommodate modern diagnostic requirements.

2. **Integration with AI models:** Incorporating this fuzzy clustering method into AI-driven frameworks-particularly hybrid models that merge traditional denoising strategies with deep learning-could further enhance denoising accuracy and adaptability to complex noise patterns.

3. **Addressing ethical and practical challenges:** As AI-driven image processing gains momentum in clinical practice, ensuring robust data privacy, regulatory compliance, and standardized protocols will be essential for successful deployment in healthcare environments.

By addressing these challenges and extending the method's capabilities, this approach has the potential to significantly enhance noise-free, high-precision medical imaging-ultimately improving diagnostic accuracy, clinical decision-making, and patient outcomes.

Ethical approval

The local research ethics committee granted ethical approval for the study.

Consent to Participate: Written informed consent was obtained from all participants prior to their involvement in the study.

Consent to Publish: Participants provided consent for their data to be used and published in scientific literature.

Authors contributions

Conceptualization: Omid Darvishi, Vafa Maihami. Methodology: Omid Darvishi, Vafa Maihami, Keyhan Khamforoosh. Project administration: Vafa Maihami. Validation: Keyhan Khamforoosh. Visualization: Omid Darvishi, Vafa Maihami, Keyhan Khamforoosh. Writing-original draft: Omid Darvishi, Vafa Maihami, Keyhan Khamforoosh.

Funding

Availability of data and materials

Data are available from the corresponding author upon reasonable request.

Conflict of interest

The authors declare no competing interests.

References

[1] Gonzalez R, Woods R. *Digital Image Processing*. 4th ed. London, UK: Pearson; 2017.

[2] Goyal B, Dogra A, Agrawal S, Sohi BS, Sharma A. Image denoising review: from classical to state-of-the-art approaches. *Information Fusion*. 2020; 55: 220-244. Available from: https://doi.org/10.1016/j.inffus.2019.09.003.

[3] Tian C, Fei L, Zheng W, Xu Y, Zuo W, Lin CW. Deep learning on image denoising: An overview. *Neural Networks*. 2020; 131: 251-275. Available from: https://doi.org/10.1016/j.neunet.2020.07.025.

[4] Sagheer SVM, George SN. A review on medical image denoising algorithms. *Biomedical Signal Processing and Control*. 2020; 61: 102036. Available from: https://doi.org/10.1016/j.bspc.2020.102036.

[5] Sakthidasan K, Nagappan NV. Noise free image restoration using hybrid filter with adaptive genetic algorithm. *Computers & Electrical Engineering*. 2016; 54: 382-392. Available from: https://doi.org/10.1016/j.compeleceng.2016.03.026.

[6] Laghari AA, Yin S. How to collect and interpret medical pictures captured in highly challenging environments that range from nanoscale to hyperspectral imaging. *Current Medical Imaging*. 2022; 18(3): 256-270. Available from: https://doi.org/10.2174/1573405617666210708123017.

[7] Srivastava V. An optimization for adaptive multi-filter estimation in medical images and EEG based signal denoising. *Biomedical Signal Processing and Control*. 2023; 82: 104513. Available from: https://doi.org/10.1016/j.bspc.2022.104513.

[8] Laghari AA, Sun Y, Alhussein M, Aurangzeb K, Anwar MS, Rashid M. Deep residual-dense network based on bidirectional recurrent neural network for atrial fibrillation detection. *Scientific Reports*. 2023; 13(1): 15109. Available from: https://doi.org/10.1038/s41598-023-42033-0.

[9] Zhang J, Niu Y, Shangguan Z, Gong W, Cheng Y. A novel denoising method for CT images based on U-net and multi-attention. *Computers in Biology and Medicine*. 2023; 152: 106387. Available from: https://doi.org/10.1016/j.compbiomed.2022.106387.

[10] Qiu D, Cheng Y, Wang X. Medical image super-resolution reconstruction algorithms based on deep learning: a survey. *Computer Methods and Programs in Biomedicine*. 2023; 238: 107590. Available from: https://doi.org/10.1016/j.cmpb.2023.107590.

[11] Wang J, Tang Y, Wu Z, Du Q, Yao L, Yang X, et al. Self-supervised guided knowledge distillation framework for unpaired low-dose CT image denoising. *Computerized Medical Imaging and Graphics*. 2023; 107: 102237. Available from: https://doi.org/10.1016/j.compmedimag.2023.102237.

[12] Göreke V. Novel method based on Wiener filter for denoising Poisson noise from medical X-ray images. *Biomedical Signal Processing and Control*. 2023; 79: 104031. Available from: https://doi.org/10.1016/j.bspc.2022.104031.

[13] Rajesh C, Kumar S. An evolutionary block based network for medical image denoising using differential evolution. *Applied Soft Computing*. 2022; 121: 108776. Available from: https://doi.org/10.1016/j.asoc.2022.108776.

[14] Diwakar M, Kumar P, Singh P, Tripathi A, Singh L. An efficient reversible data hiding using SVD over a novel weighted iterative anisotropic total variation based denoised medical images. *Biomedical Signal Processing and Control*. 2023; 82: 104563. Available from: https://doi.org/10.1016/j.bspc.2023.104563.

[15] Lyu J, Sui B, Wang C, Dou Q, Qin J. Adaptive feature aggregation based multi-task learning for uncertainty-guided semi-supervised medical image segmentation. *Expert Systems with Applications*. 2023; 232: 120836. Available from: https://doi.org/10.1016/j.eswa.2023.120836.

[16] Maihami V, Yaghmaee F. A genetic-based prototyping for automatic image annotation. *Computers & Electrical Engineering*. 2018; 70: 400-412. Available from: https://doi.org/10.1016/j.compeleceng.2017.07.016.

[17] Maihami V, Yaghmaee F. A review on the application of structured sparse representation at image annotation. *Artificial Intelligence Review*. 2017; 48(3): 331-348. Available from: https://doi.org/10.1007/s10462-016-9492-8.

[18] Krinidis S, Chatzis V. A robust fuzzy local information C-means clustering algorithm. *IEEE Transactions on Image Processing*. 2010; 19(5): 1328-1337. Available from: https://doi.org/10.1109/TIP.2010.2046903.

[19] Das S, Adhikary A, Laghari AA, Mitra S. Eldo-Care: EEG with Kinect sensor based telehealthcare for the disabled and the elderly. *Neuroscience Informatics*. 2023; 3(2): 100130. Available from: https://doi.org/10.1016/j.neuri.2023.100130.

[20] Saeed U, Kumar K, Khuhro MA, Laghari AA, Shaikh AA, Rai A. DeepLeukNet-a CNN based microscopy adaptation model for acute lymphoblastic leukemia classification. *Multimedia Tools and Applications*. 2023; 82(5): 6543-6567. Available from: https://doi.org/10.1007/s11042-022-13597-2.

[21] Paris S, Durand A. A fast approximation of the bilateral filter using a signal processing approach. *International Journal of Computer Vision*. 2009; 81: 24-52. Available from: https://doi.org/10.1007/s11263-008-0160-6.

[22] Dunn JC. A fuzzy relative of the ISODATA process and its use in detecting compact well-separated clusters. *Journal of Cybernetics*. 1973; 3(3): 32-57. Available from: https://doi.org/10.1080/01969727308546046.

[23] Bezdek JC. *Pattern Recognition with Fuzzy Objective Function Algorithms*. New York, NY, USA: Plenum Press; 1981.

[24] Zadeh LA. Fuzzy sets. *Information and Control*. 1965; 8(3): 338-353. Available from: https://doi.org/10.1016/S0019-9958(65)90241-X.

[25] Wu C, Chen Y. Adaptive entropy weighted picture fuzzy clustering algorithm with spatial information for image segmentation. *Soft Computing*. 2020; 86: 1-23. Available from: https://doi.org/10.1007/s00500-020-05128-8.

[26] Feng C, Li W, Hu J, Yu K, Zhao D. BCEFCM_S: bias correction embedded fuzzy c-means with spatial constraint to segment multiple spectral images with intensity inhomogeneities and noises. *Signal Processing*. 2020; 168: 1-21. Available from: https://doi.org/10.1016/j.sigpro.2019.107342.

[27] Halder A, Nandi A. Robust brain magnetic resonance image segmentation using modified rough-fuzzy c-means with spatial constraints. *Applied Soft Computing*. 2019; 85: 1-17. https://doi.org/10.1016/j.asoc.2019.105524.

[28] Lei T, Jia X, Zhang LY, He H, Meng H, Nandi AK. Superpixel-based fast fuzzy c-means for color image segmentation. *IEEE Transactions on Fuzzy Systems*. 2019; 27(9): 1753-1766. Available from: https://doi.org/10.1109/TFUZZ.2019.2895563.

[29] Zhang H, Bruzzone L, Shi W, Hao M, Wang Y. Enhanced spatially constrained remotely sensed imagery classification using a fuzzy local double neighborhood information c-means clustering algorithm. *IEEE Journal of Selected Topics in Applied Earth Observations and Remote Sensing*. 2018; 11(8): 2896-2910. Available from: https://doi.org/10.1109/JSTARS.2018.2849392.

[30] Barrah H, Cherkaoui A, Sarsri D. Robust FCM algorithm with local and gray information for image segmentation. *Advances in Fuzzy Systems*. 2016; 2016: 2378430. Available from: https://doi.org/10.1155/2016/2378430.

[31] Elazab A, Wang C, Jia F, Wu J, Li G, Hu Q. Segmentation of brain tissues from magnetic resonance images using adaptively regularized kernel-based fuzzy c-means clustering. *Computational and Mathematical Methods in Medicine*. 2015; 2015: 485495. Available from: https://doi.org/10.1155/2015/485495.

[32] Shi P, Guo L, Cui H, Chen L. Geometric consistent fuzzy cluster ensemble with membership reconstruction for image segmentation. *Digital Signal Processing*. 2023; 134: 103901. Available from: https://doi.org/10.1016/j.dsp.2023.103901.

[33] Cui Y, Huang H, Liu J, Zhao M, Li C, Han X, et al. FFCM-MRF: An accurate and generalizable cerebrovascular segmentation pipeline for humans and rhesus monkeys based on TOF-MRA. *Computers in Biology and Medicine*. 2024; 170: 107996. Available from: https://doi.org/10.1016/j.compbiomed.2023.107996.

[34] Wei T, Wang X, Li X, Zhu S. Fuzzy subspace clustering noisy image segmentation algorithm with adaptive local variance & non-local information and mean membership linking. *Engineering Applications of Artificial Intelligence*. 2022; 110: 104672. Available from: https://doi.org/10.1016/j.engappai.2022.104672.

[35] Song S, Jia Z, Shi F, Wang J, Ni D. Adaptive fuzzy weighted C-mean image segmentation algorithm combining a new distance metric and prior entropy. *Engineering Applications of Artificial Intelligence*. 2024; 131: 107776. Available from: https://doi.org/10.1016/j.engappai.2024.107776.

[36] Bose A, Maulik U, Sarkar A. An entropy-based membership approach on type-II fuzzy set (EMT2FCM) for biomedical image segmentation. *Engineering Applications of Artificial Intelligence*. 2024; 127: 107267. Available from: https://doi.org/10.1016/j.engappai.2023.107267.

[37] Aetesam H, Maji SK. Deep variational magnetic resonance image denoising via network conditioning. *Biomedical Signal Processing and Control*. 2024; 95: 106452. Available from: https://doi.org/10.1016/j.bspc.2024.106452.

[38] Xu R, Xu Y, Yang X, Huang H, Lei Z, Quan Y. Wavelet analysis model inspired convolutional neural networks for image denoising. *Applied Mathematical Modelling*. 2024; 125: 798-811. Available from: https://doi.org/10.1016/j.apm.2023.09.017.

[39] Zhang B, Zhang Y, Wang B, He X, Zhang F, Zhang X. Denoising swin transformer and perceptual peak signal-to-noise ratio for low-dose CT image denoising. *Measurement*. 2024; 227: 114303. Available from: https://doi.org/10.1016/j.measurement.2023.114303.

[40] Torun O, Esen Yuksel S, Erdem E, Imamoglu N, Erdem A. Hyperspectral image denoising via self-modulating convolutional neural networks. *Signal Processing*. 2024; 214: 109248. Available from: https://doi.org/10.1016/j.sigpro.2023.109248.

[41] Zhang R, Yu Z, Sheng Z, Ying J, Cao SY, Chen SJ, et al. SGDFormer: one-stage transformer-based architecture for cross-spectral stereo image guided denoising. *Information Fusion*. 2025; 113: 102603. Available from: https://doi.org/10.1016/j.inffus.2024.102603.

[42] Feruglio PF, Vinegoni C, Gros J, Sbarbati A, Weissleder R. Block matching 3D random noise filtering for absorption optical projection tomography. *Physics in Medicine & Biology*. 2010; 55(18): 5401-5415. Available from: https://doi.org/10.1088/0031-9155/55/18/006.

[43] Zhao T, McNitt-Gray M, Ruan D. A convolutional neural network for ultra-low-dose CT denoising and emphysema screening. *Medical Physics*. 2019; 46(9): 3941-3950. Available from: https://doi.org/10.1002/mp.13665.

[44] Chen H, Zhang Y, Kalra MK, Lin F, Chen Y, Liao P. Low-dose CT with a residual encoder-decoder convolutional neural network. *IEEE Transactions on Medical Imaging*. 2017; 36(12): 2524-2535. Available from: https://doi.org/10.1109/TMI.2017.2715284.

[45] Tseng KK, Zhang R, Chen CM, Hassan MM. DNetUnet: a semi-supervised CNN for medical image segmentation in supercomputing AI services. *The Journal of Supercomputing*. 2021; 77(4): 3594-3615. Available from: https://doi.org/10.1007/s11227-020-03399-4.

[46] Wang EK, Chen CM, Hassan MM, Almogren A. A deep learning-based medical image segmentation technique in the Internet-of-Medical-Things domain. *Future Generation Computer Systems*. 2020; 107: 135-144. Available from: https://doi.org/10.1016/j.future.2020.01.055.

[47] Younas R, Haq HBU, Baig MD. A framework for extensive content-based image retrieval system incorporating relevance feedback and query suggestion. *Spectrum of Operational Research*. 2024; 1(1): 13-32. Available from: https://doi.org/10.31181/sor1120242.

[48] Ravichandran KS. Estimation of automatic license plate recognition using deep learning algorithms. *Spectrum of Decision Making and Applications*. 2025; 2(1): 100-119. Available from: https://doi.org/10.31181/sdmap21202512.

[49] Citroni R, Mangini F, Frezza F. Efficient integration of ultra-low power techniques and energy harvesting in self-sufficient devices: a comprehensive overview of current progress and future directions. *Sensors*. 2024; 24(14): 4471. Available from: https://doi.org/10.3390/s24144471.

[50] Zhang X, Ning Y, Li X, Zhang C. Anti-noise FCM image segmentation method based on quadratic polynomial. *Signal Processing*. 2021; 178: 107767. Available from: https://doi.org/10.1016/j.sigpro.2020.107767.

[51] Coupé P, Yger P, Prima S, Hellier P, Kervrann C, Barillot C. An optimized blockwise nonlocal means denoising filter for 3-D magnetic resonance images. *IEEE Transactions on Medical Imaging*. 2008; 27(4): 425-441. Available from: https://doi.org/10.1109/TMI.2007.906087.

[52] Manjón JV, Coupé P, Martí-Bonmatí L, Collins DL, Robles M. Adaptive nonlocal means denoising of MR images with spatially varying noise levels. *Journal of Magnetic Resonance Imaging*. 2010; 31(1): 192-203. Available from: https://doi.org/10.1002/jmri.22003.

[53] Coupé P, Manjón JV, Robles M, Collins DL. Adaptive multiresolution nonlocal means filter for three-dimensional magnetic resonance image denoising. *IET Image Processing*. 2012; 6(5): 558-568. Available from: https://doi.org/10.1049/iet-ipr.2011.0232.

[54] Manjón JV, Coupé P, Buades A, Collins DL, Robles M. New methods for MRI denoising based on sparseness and self-similarity. *Medical Image Analysis*. 2012; 16(1): 18-27. Available from: https://doi.org/10.1016/j.media.2011.04.003.

[55] Luisier F, Blu T, Wolfe PJ. A CURE for noisy magnetic resonance images: Chi-square unbiased risk estimation. *IEEE Transactions on Image Processing*. 2012; 21(8): 3454-3466. Available from: https://doi.org/10.1109/TIP.2012.2191562.

[56] Foi A. Noise estimation and removal in MR imaging: the variance-stabilization approach. In: *2011 IEEE International Symposium on Biomedical Imaging: From Nano to Macro*. Chicago, CA, USA: IEEE; 2011. p.1809-1814.

[57] López-Rubio E, Florentín-Núñez MN. Kernel regression based feature extraction for 3D MR image denoising. *Medical Image Analysis*. 2011; 15(4): 498-513. Available from: https://doi.org/10.1016/j.media.2011.02.005.

[58] Chung H, Lee ES, Ye JC. MR image denoising and super-resolution using regularized reverse diffusion. *IEEE Transactions on Medical Imaging*. 2022; 42(4): 922-934. Available from: https://doi.org/10.1109/TMI.2022.3225037.

[59] Zhang K, Zuo W, Chen Y, Meng D, Zhang L. Beyond a Gaussian denoiser: residual learning of deep CNN for image denoising. *IEEE Transactions on Image Processing*. 2017; 26(7): 3142-3155. Available from: https://doi.org/10.1109/TIP.2017.2662206.

[60] Ran M, Hu J, Chen Y, Chen H, Sun H, Zhou J, et al. Denoising of 3D magnetic resonance images using a residual encoder-decoder Wasserstein generative adversarial network. *Medical Image Analysis*. 2019; 55: 165-170. Available from: https://doi.org/10.1016/j.media.2019.04.010.

[61] Xu Y, Han K, Zhou Y, Wu J, Xie X, Xiang W. Deep adaptive blending network for 3D magnetic resonance image denoising. *IEEE Journal of Biomedical and Health Informatics*. 2021; 25(7): 2633-2644. Available from: https://doi.org/10.1109/JBHI.2021.3055114.

[62] Aetesam H, Maji SK. Deep variational magnetic resonance image denoising via network conditioning. *Biomedical Signal Processing and Control*. 2024; 95: 106452. Available from: https://doi.org/10.1016/j.bspc.2024.106452.